2020

Preliminary Design and Analysis of a Wave Energy Converter with Electromagnetic Induction

Laura Fernandez de Valderrama
University of North Florida, n01421906@unf.edu

Preliminary Design and Analysis of a Wave Energy Converter with Electromagnetic Induction

Laura Fernandez de Valderrama

A thesis submitted in partial fulfillment of the requirements

For the degree of Master of Science in Civil Engineering with a concentration

In Coastal and Port Engineering

College of Computing, Engineering, and Construction

University of North Florida

May 2020

Sponsored by

Taylor Engineering Research Institute (TERI)

Chairperson of the Supervisory Committee:

Professor Cigdem Akan

Department of Civil Engineering

Members of the Supervisory Committee:

Professor Don Resio

Department of Civil Engineering

Professor Brian Kopp

Department of Electrical Engineering

Thesis entitled “Preliminary Design and Analysis of a Wave Energy Converter with Electromagnetic Induction” by Laura Fernandez de Valderrama is approved:

_____ _____

Committee Chair: Dr. Cigdem Akan

_____ _____

Committee Member: Dr. Don Resio

_____ _____

Committee Member: Dr. Brian Kopp

Accepted for the School of Engineering:

_____ _____

Department Chair: Dr. Osama Jadaan

Accepted for the College of Computing, Engineering and Construction:

_____ _____

College Dean: Dr. Chip Klostermeyer

Accepted for the University:

_____ _____

Dean of the Graduate School: Dr. John Kantner

ABSTRACT

As the energy demand increases with the constantly increasing population, as well as the effort to replace conventional fossil fuels with cleaner sources of energy, ocean energy has emerged as a potential global resource. The ocean contains an enormous amount of energy that has not been exploited yet, although efforts have augmented during the past decades.

The overall purpose of this research is to design, model, and analyze, a wave energy converter (WEC) prototype to contribute to the current research in this field. This particular work represents the first stage of the research process in which the ultimate goal is to introduce a WEC prototype that can overcome previous challenges, and/or improve energy harnessing from previous models.

The focus of this paper is to study previous wave energy systems, both successful and unsuccessful, investigate what has been done up to date, and perform a numerical model analysis of two different body shapes and at two different water depths. Also, a local case study of ocean wave's conditions is performed. The objective is to compute the design parameters of the working environment and to analyze both numerical models, so that a small-scale model of the prototype can be implemented in the next phase of this research and tested experimentally.

ACKNOWLEDGMENTS

Firstly, I would like to express my deepest thanks and most sincere appreciation to my advisor Dr. Cigdem Akan, for all the support and guidance that she has provided me throughout the entire process. Thank you, Dr. Akan, for your valuable knowledge and advice that has helped me through my thesis. Also, I am thankful for the effort she has made to make this work, especially during the last few weeks when the school closed due to COVID-19 and we had to transition to remote instruction.

I would also like to thank the University of North Florida's School of Engineering, College of Computing, Engineering, and Construction (CCEC), as well as the Taylor Engineering Research Institute (TERI) for making this program possible. Additionally, I would like to thank in particular professors Don Resio and Brian Kopp, for all the time and effort they have offered during this research.

TABLE OF CONTENTS

LIST OF FIGURES

LIST OF TABLES

LIST OF APPENDICES

NOMENCLATURE

h	water depth
H	wave height
Hs	significant wave height
T	wave period
T_p	dominant wave period
λ	wavelength
C	wave celerity
A	wave amplitude
ω	angular wave frequency
η	surface elevation
ϕ	velocity potential
ρ	water density
m	mass of the body
g	acceleration due to gravity
$\forall$	displaced volume
Zo	wetted height of the body
W	weight of the body
Fb	buoyancy force
Fu	uplifting force
P	net pressure force
ω_n	natural frequency
I	induced current by a magnetic field

V	generated voltage by a magnetic field
D	diameter
A_c	cross-sectional area
B	magnetic field
μ_o	magnetic permeability of free space ($4\pi\ 10^{-7}$ H/m)
N	number of coils
C_d	drag coefficient
C_i	inertia coefficient
C_a	added mass coefficient
Ω	volume of the element per unit length (m^3/m)
a_w	acceleration of the flow (m/s^2)
$\ddot{X}$	acceleration of the body (m/s^2)
U	relative velocity between the flow and the body
F_{FK}	Froude-Krylov Force
F_I	diffraction Force
F_R	radiation Force
F_D	drift Force

1. Introduction

1.1.Context

The elevated energy demand, along with the rising environmental concern to reduce carbon emissions, has driven researchers to invest in and develop renewable and cleaner sources of energy. With a current population of over 7.5 billion people, and continuously increasing at an estimated rate of 1-1.5% per year, the worldwide energy consumption is also projected to keep growing in the following years (U.S. Census Bureau, 2019).

The global electricity consumption for 2018 was almost 23,000 TWh (Terawatt-hour), where the U.S. placed second only after China, with almost 4,000 TWh of consumed electric power (Global Energy Statistical Yearbook, 2019). Of the total electricity consumed in the U.S., almost 64% came from fossil fuels (petroleum, coal, and natural gas), 19% from nuclear, and 17% from renewable energies, including bioenergy, hydroelectric, wind, solar, and geothermal. A breakdown of the electricity consumption by source in the U.S. obtained from the Energy Information Administration (EIA) is shown in Figure 1 (EIA, 2019).

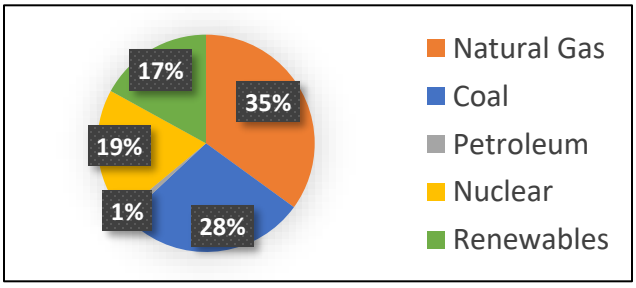

Figure 1. United States energy consumption by source in 2018 (EIA, 2019)

In fact, fossil fuels are not only the main resource in the United States but also worldwide. It is well known that burning fossil fuels release large quantities of carbon dioxide

and other pollutants that can lead to the greenhouse effect. Moreover, fossil fuel reserves are non-renewable, which means that they do not regenerate, or they take thousands of years to do so. For these reasons, the effort of reducing both greenhouse gases emissions and the reliability on limited resources has motivated the necessity of exploiting cleaner and renewable alternative sources of energy.

On the other hand, renewable resources are unlimited, safe, and available anywhere. The wide variety of resources allows each region to exploit one source or another based on the theoretical potential at that specific location. However, there are still significant challenges that renewable energies need to overcome. The major barrier that renewable technologies are facing to compete with the already established fossil fuels is the economic feasibility.

According to the International Renewable Energy Agency (IRENA), the cost of renewable energy is falling and will continue to fall within the next few years, up to the point where they will be a consistent and cheaper source of electricity than traditional fossil fuels (IRENA, 2014). For instance, wind and solar energies have been developed during the past few decades and have reduced their cost an average of 25% and 75% respectively, between 2009 and 2017 (IRENA, 2018). However, these resources are still capital intensive and have important limitations such as location and availability.

Alternatively, ocean energy is vast, unlimited, consistent, and is readily available. Moreover, water is 850 times denser than air, which results in a much higher potential for power generation (Falnes, 2007). Ocean power can be harnessed in different forms, being tidal and wave energy the most important ones. Tides are created by the gravitational pull from both the moon and the sun, and there are two forms of harvesting tidal energy; (1) tidal range, using a barrage or other

barrier to extract power from the height difference between high and low tides; and (2) tidal current (or tidal stream), by using turbines and generators placed underwater to capture the kinetic motion from the rise and fall of the tides (IRENA, 2014).

Wave energy, which is the focus of this thesis, harnesses the kinetic energy from the motion of the ocean waves. Ocean waves are generated by wind, which is a product of solar energy. Solar energy has an average intensity of 0.1 – 0.3 kW/m^2 horizontal surface on earth, which is then transformed into wind with an increased power flow intensity of 0.5 kW/m^2 envisaged area. As the wind is converted to wave energy, even more spatial concentration takes place. The average power flow intensity just below the ocean surface is approximately 2-3 kW/m^2, although this varies with wave climate (Falnes, 2007). Therefore, wave energy can be considered a concentrated form of solar power. Moreover, wind and solar are only available about 20-30% of the time, whereas wave power is estimated to be readily available about 90% of the time (Pelc & Fujita, 2002). There are different ways in which power can be harvested from waves, described more deeply in the Literature Review (Section 2).

This paper is structured as follows; Section 2 covers a literature review about wave energy and wave energy converters, followed by the methodology chosen for this work in Section 3. Next, Section 4 introduces the proposed model, and Section 5 describes the design concepts for the proposed model. Then, the modeling approach and numerical model simulations are presented in Sections 7, followed by the environmental impacts in Section 8. The economic analysis of the system is provided in Section 9. Lastly, section 10 wraps up with the conclusion, and Section 11 describes the future work that needs to be done.

1.2. Motivation/Objectives

The motivation for this research is to analyze the current situation of wave energy technologies, in order to develop a sustainable system that can contribute to the research in this field. The objective is therefore to design and model a system capable of harnessing energy from the waves economically and efficiently.

1.3 Organization of the Thesis

The following procedure was proposed to achieve the purpose of this work: first, to review and evaluate previous wave energy converter devices. Next, to study wave theory and wave energy calculations to obtain a better understanding of wave's behavior, and to assess wave characteristics and wave energy potential at the selected location for the work. Then, the proposed model is presented. A numerical simulation of a simplistic, small-scale model of the device was created to analyze its performance, study the wave-body interaction, and investigate different types of moorings for the device. Lastly, an economic study of the system was conducted to estimate the economic feasibility of the proposed device, compare it with other current wave energy systems, and analyze why or why not it is feasible.

2. Literature Review

This literature review provides an evaluation of the ocean energy resource and potential, as well as an overview of the different types of wave energy converters. Overall, the purpose of this literature review is to provide background information about wave's behavior and wave energy systems, as well as a basic understanding of what has been developed so far, what is the current status of the research, and what future work needs to be done. Additionally, the historical review

of existing wave energy models helps to better comprehend the working principle of converting wave energy into electricity.

2.1. Ocean Energy Resource

The ocean's power intensity varies with vary with latitude, seasons, and other weather and climate conditions. However, both tidal and wave potential can be forecasted. Borthwick and other researchers estimated a theoretical tidal energy potential of 26,000 TWh, and 32,000 TWh for wave energy, being both of their actual technical potential quite lower (Sims et al. 2007 & Mørk et al. 2010, as cited in Borthwick, 2016). Other research differs slightly from these estimates, although all agree that wave energy potential is considerably higher than tidal energy potential. Even though both tidal and wave technologies are capital intensive and still at a very early stage of maturity, tidal energy systems are less sophisticated, which makes them less expensive. Thus, tidal energy currently stands at a slightly more developed stage. Nevertheless, wave energy potential is considerably higher than tidal energy and has a more consistent and greater efficiency than tidal systems.

The estimated theoretical ocean resource potential in the United States is presented in Table 1, with data obtained from the U.S. Department of Energy in the 2015 Quadrennial Technology Review (U.S.DOE, 2019).

Table 1. Estimated ocean resource potential in the United States (2015 Quadrennial Technology Review)

Resource Assessment	Theoretical Potential	Technical Potential
Waves	1,600–2,640 TWh/year	900–1,230 TWh/year
Tidal Streams	445 TWh/year	222–334 TWh/year

Tidal Currents	200 TWh/year	45–163 TWh/year
Total (average)	2,762 TWh/year	1,445 TWh/year

Both the theoretical and the technical potential for wave energy are significantly higher than the tidal stream and tidal current potential combined. By taking the average of each interval, it is determined that wave energy represents 77% of the theoretical potential, and 74 % of the technical potential. Additionally, the theoretical worldwide wave energy potential is estimated to be of the same order of magnitude as the world's electrical consumption. Studies from the Intergovernmental Panel on Climate Change (IPCC) and the U.S. DOE, reported a theoretical potential of wave power of 29,500 TWh/year, considering all areas with wave energy densities higher than 5 kW/m (U.S.DOE, 2019). Just within the U.S., the theoretical resource potential ranges between 1,600 and 2,640 TWh/year (U.S.DOE, 2019). The range of wave energy potential fluctuates between 15-75 kW/m, and offshore sites may easily exceed 30–40 kW/m wave power density (IRENA, 2019). Additionally, IRENA estimates that 2% of the world's coastline also exceeds an average density of 30 kW/m (IRENA, 2019).

For these reasons, due to the tremendous untapped potential and the technological gap between tidal and wave technologies, the concentration of this work is particularly wave energy. The global wave power density potential is illustrated in Figure 2, where the maximum power density is encountered in the Indian Ocean region, with an estimated 127.7 kW/m (Rusu & Onea, 2017).

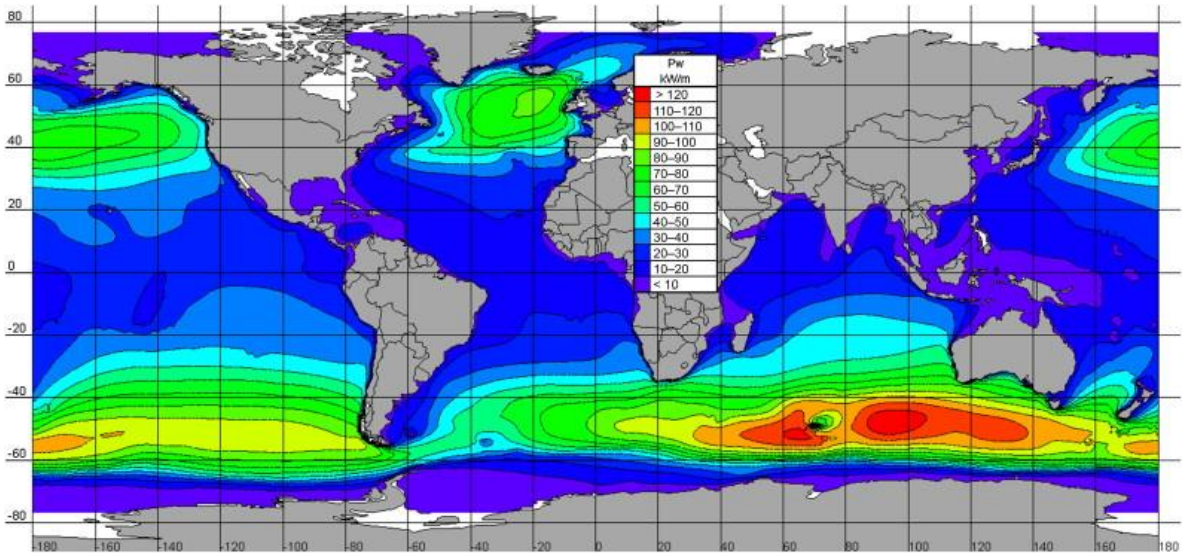

Figure 2. Map of the Theoretical Mean Power Density Potential (kW/m) (EIA, 2019)

The more abundant wave energy potential is found on the western coast of the continents, especially between the 30º and 60º latitudes. Although predictions are promising, wave energy technologies are still at a very immature stage of development due to the lack of experience in the field, the numerous uncertainties of the working environment, the elevated cost, difficulty for accessibility, maintenance and survivability, and the extreme weather conditions. A review of the most relevant wave energy converters up to date and their working principle is presented in the following section.

2.2. Review of Wave Energy Converter Systems

As new technologies are developing, wave energy has overcome the prohibitive elevated initial investment of a wave energy system, and smaller prototypes are already being tested. However, only a few of these prototypes have been commercialized yet. The goal is to overcome these major challenges and make wave energy a feasible and cost-competitive alternative to current resources.

Wave energy converters can be classified by their location; they are divided into onshore, nearshore, or offshore devices. The higher amount of energy potential is found in deep water, where the significant wave height is higher. However, offshore devices are more expensive to construct and maintain, have difficult accessibility, and need to withstand more extreme conditions. Because of the challenges that offshore devices have to face, most models up to date have been designed and tested for nearshore and onshore. The wave energy converter proposed in this thesis would also operate in the nearshore.

Also, WECs are distinguished by their working principle, and the main types include point absorber, oscillating water column, attenuator, and terminator.

A. Point Absorber

A point absorber is a floating device with small dimensions compared to the incident wavelength, which absorbs energy from the vertical motion of the device as the wave passes through. This vertical motion is converted into rotational motion by compressing a gas or liquid inside the chamber, powering a generator that charges an energy storage system, and therefore producing electricity. Below are some examples of point absorber devices.

Ocean Power Technologies (OPT) has been testing PowerBuoy off New Jersey and Hawaii since it was founded in 1994. The first commercial prototype of PowerBuoy, shown in Figure 3, was a 40 kW buoy installed in 2005 one mile off the coast of Hawaii at the Marine Corps base in Kaneohe Bay, Oahu (about 30 meters deep). It has a diameter of 3 meters approximately, is almost 20 meters long, and weighs about 10 tons. It was connected to the grid for the first time in 2010, and ever since deployment OPT has been working along with the Navy in testing and

improving PowerBuoy prototypes. After successfully providing power to coastal networks and surviving hurricane Irene in 2011, OPT launched its commercial PB3 PowerBuoy four miles off the coast of New Jersey in 2016. It produces 300 W of continuous power, depending on ocean conditions, with peaks of up to 7.2 kW (OPT, 2016).

Figure 3. Picture of Power Buoy off Hawaii (OPT, 2016)

OPT planned a project off Oregon, consisting of ten PB50 PowerBuoy of 150 kW capacity and a weight of 200 tons, giving a total capacity of 1.5 MW. The estimated investment for this wave farm was about $64 million and was expected to generate 4,140MWh/yr. However, after launching the first PB50, a study confirmed that the scale of the project was not viable and economically not feasible (Dr. Mekhiche, 2016). OPT withdrew from the Reedsport Wave Power, and the remaining nine devices were never installed. OPT has currently other operating projects in Australia and Europe (OPT, 2016), and a picture of the PowerBuoy P150 is provided in Figure 4.

Figure 4. Picture of P150 Power Buoy off Scotland (OPT, 2016)

Figure 5 shows Azura, a 45-ton point absorber that has a 360-degree rotating float mechanism to extract power from both the vertical and horizontal motions of waves (heave and surge, respectively). It was deployed off Hawaii in 2012 by Northwest Energy Innovations (NWEI), after several years of testing a half-scale prototype off the coast of Oregon. Azura has a 20 kW capacity and is currently operating and supplying energy to the Marine Corps base on the island while being tested by the University of Hawaii and with the support from the US Navy (NWEI, 2015). The Azura commercial prototype was a successful one-half scale demonstration program with a target of levelized cost of energy of less than $0.5/kWh, according to NWEI Founder and CEO Steve Kopf (Kopf, 2016). The estimated capital cost of Azura was approximately $10 million, and according to the Ocean Energy Council and the EIA, Azura can reach a performance of $0.075/kWh at best (U.S. EIA, 2015).

Figure 5. Picture of Azura at the Navy's Wave Energy Site at Hawaii (NWEI, 2015)

B. Oscillating Water Column (OWC)

An oscillating water column is a partially submerged hollow chamber open to the ocean below the waterline. As the water column rises and falls within the chamber, the trapped air drives a turbine connected to a generator, similar to a piston compression cycle (Falcao, 2014). The working principle of an OWC device is depicted below in Figure 6.

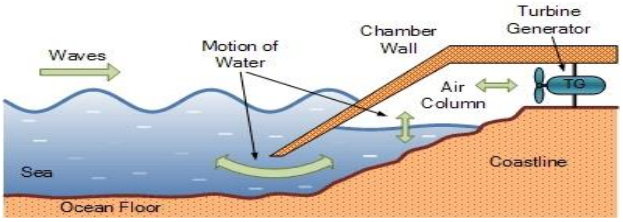

Figure 6. Working principle of an Oscillating Wave Energy Converter

Examples of oscillating water column devices are provided below. The Limpet, shown in Figure 7, was the first commercial wave plant in the world. Designed by WaveGen, the Limpet was a 500 kW oscillating water column installed off Islay, Scotland, in 2000. It was deployed after the decommissioning of a 75 kW prototype at The Queen's University of Belfast, that had been testing since 1991 (Boake, Whittaker, & Folley, M. 2002). Unfortunately, the plant ended up closing in 2012, and all installations except the concrete construction have been removed (Islay Limpet, 2018).

Figure 7. Picture of the LIMPET in Islay, Scotland

Mutriku Wave Power Plant, shown in Figure 8, is an OWC power plant built into a breakwater off the coast of Spain, also designed by WaveGen. The design was completed in 2006, and Mutriku was officially opened in July 2011. With an installation of 16 turbines of 18.5 kW capacity each, it supplies an output of almost 300 kW. Mutriku has been successfully operating since then, supplying almost 2 GWh of electricity up to 2018 (Torre-Enciso, Ortubia,

Lopez de Aguileta, & Marques, 2009). The estimated cost of the project was € 6.4 million ($8 million), and it is estimated to reduce carbon emissions by 600 tons per year (Bald, 2019).

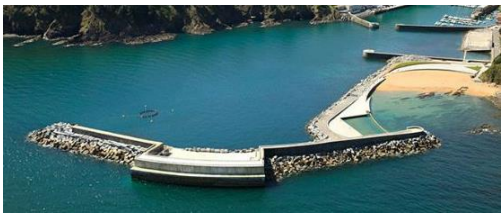

Figure 8. Picture of the Mutriku Wave Power Plant, Spain

C. Attenuator

An attenuator is a long floating device composed of multiple cylinders connected by hinges or joints, which operates parallel to the predominant wave direction, harnessing energy from the relative motion of the waves (Drew Plummer, & Sahinkaya, 2009).

The most notorious attenuator device is the Pelamis, which is a semi-submerged articulated structure with four cylindrical segments hinged together by joints. The relative motion of the waves is converted into hydraulic pressure at each hinged connection before it is transformed into electricity through a set of internal accumulators and twin generators (Anderson, 2003).

The first Pelamis P1 full-scale prototype, shown in Figure 9, was installed off Portugal in 2004 by Ocean Power Delivery (OPD), and became the world's first offshore device to be commercialized and successfully generate electricity into the national grid (Jarocki, 2010). The first stage of Pelamis Wave Power consisted of the deployment of three Pelamis P1 models of 0.75 MW each, with an initial investment of 8.2 million euros (about $9m). Each device had a total length of 120 meters, a diameter of almost 4 meters, and a weight of 760 tons. The Pelamis P1 devices were designed to operate offshore, ideally between 50 to 60 meters depth (Thomson,

Chick, & Harrison, 2018). The farm was successfully implemented, and in September of 2008 was delivering 2.25 MW of power to the national grid. Unfortunately, after four months of operation, the three machines had to be towed back due to technical problems. The farm was never re-installed, and with the planning of a second phase consisting of 28 more Pelamis devices, Pelamis Wave Power went into administration and ended up being decommissioned in 2014 (EMEC, 2017).

Figure 9. Picture of the P1 from Pelamis Wave Power (EMEC, 2012)

D. Terminator / Overtopping Devices

A terminator, also called overtopping device, is a large structure that operates perpendicular to the wave direction. Incident waves break into an elevated reservoir, where they are returned to the ocean passing through a conventional turbine, converting the potential energy into electricity (Li& Yu, 2012). The working principle of an overtopping device is illustrated in Figure 10.

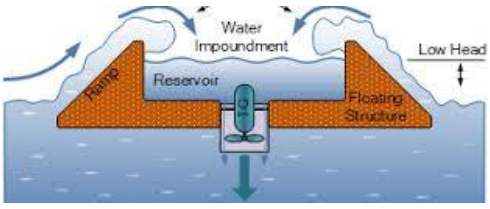

Figure 10. Working principle of an Overtopping Wave Energy Converter

The most significant terminator device is The Wave Dragon, shown in Figure 11. Wave Dragon is a floating device that represented a unique way of capturing wave energy with very

few moving parts (Jarocki, 2010). It is made of a combination of steel and reinforced concrete, and the two reflector arms concentrate the power of oncoming waves and direct water flow up into a raised basin. The water returns to the sea through a battery of low-head turbines that harness the potential energy (Sørensen & Friis-Madsen, 2015).

Wave Dragon started with a 1:50 scale prototype of a 1.5 MW model at Aalborg University (Denmark). After over 20,000 hours of testing between 1998 and 2002 and $1.1 million invested, Wave Dragon designed a 1:4.5 prototype. This unit rated at 20 kW was deployed at the North Sea off Denmark in 2003, at the Danish Wave Energy. Its cost was approximately $5.5 million and became the world's first offshore floating device supplying electricity to the grid. The tests verified an average annual 18% wave-to-wire efficiency for a full-scale device, 2% more than predicted at this stage (Sørensen & Friis-Madsen, 2015). Wave Dragon then expected to grow and developed a 1.5 MW demonstrator at the pre-commercial stage with a focus on designing a 4 MW and 7 MW units. The 4 MW device required a water depth of 25 m or higher and had a reservoir with capacity for 8,000 m^3 of water. Then, a 7 MW unit was projected to be deployed at the Celtic Sea between 2010 and 2012, with an estimated cost of $28 million. However, the device was never deployed and Wave Dragon closed in 2015 (Wave Dragon, 2016).

Figure 11. Picture of the 20kW Wave Dragon model. (Wave Dragon, 2016)

3. Methodology

3.1. Governing Equations

Three-dimensional, three directional wave kinematics can be described by a velocity potential (ϕ). For any ideal fluid, i.e. irrotational and incompressible, a velocity potential exists that satisfies the continuity equation, or Laplace equation, shown in Equation 1 (Dean & Dalrymple, 1991).

$$\nabla^2 \Phi = \frac{\partial^2 \Phi}{\partial x^2} + \frac{\partial^2 \Phi}{\partial y^2} + \frac{\partial^2 \Phi}{\partial z^2} = 0 \quad (1)$$

where $u = \frac{\partial \Phi}{\partial x}$, $v = \frac{\partial \Phi}{\partial y}$ and $w = \frac{\partial \Phi}{\partial z}$

The boundary conditions are:

1. Bottom Boundary Condition (BBC): the velocity at the seabed is 0 or negligible.
2. Periodicity: wave repeats forever, i.e., frictionless, no bottom effects.
3. Kinematic Free Surface Boundary Condition (KFSBC): states that the particles on the surface stay on the surface, representing the boundary between two different fluids, in this case, water and air.
4. Dynamic Free Surface Boundary Condition (DFSBC): states that the pressure on the surface must remain uniform along the wave (Bernoulli Equation).

Depending on the way of treatment of the kinematic and dynamic free surface boundary conditions, wave theories can be divided generally into two wide categories of *Linear* and *Nonlinear*.

3.2. Wave Theory

There are three main types of ocean waves: wind waves, tides, and tsunamis. Wind waves are waves generated by the wind blowing over the ocean's surface; tidal waves, are produced by

gravitational forces, mostly from the moon and the sun with the Earth; and tsunami waves are the ones produced by the displacement and forces of tectonic plates (Toffoli & Bitner-Gregersen, 2017). The most common type of wave is wind-driven or *airy waves*.

There are many different approaches to describe wind waves, including regular and irregular wave spectra. For this work, linear wave theory and wave spectra are used. Linear wave theory can be used for a basic understanding and a simplistic approach to wave behavior, whereas for a more realistic approach, wave spectra must be used. Both approaches are discussed below.

3.2.1 Linear Wave Theory

Linear wave theory is the simplest of all approaches. It defines ocean waves as a monochromatic wave, which means a single frequency wave. Linear waves are described as a sine function, shown in Figure 12. In real ocean waves, the crest is sharper and the trough is smoother than in linear sine waves.

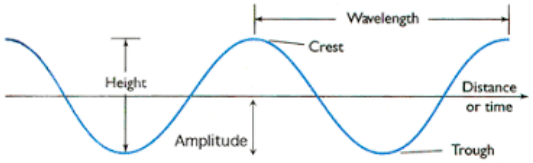

Figure 12. Linear Wave Characteristics (Dean & Dalrymple, 1991)

In linear wave theory, all nonlinear boundary conditions are linearized, and the problem turns to solve a linear second-order differential equation under the application of linear boundary conditions.

Kinematic and dynamic free surface boundary conditions are then described as

$$\frac{\partial \eta}{\partial \mathrm{t}} = \frac{\partial \Phi}{\partial \mathrm{z}} \tag{2}$$

$$\frac{\partial \Phi}{\partial t} + \frac{1}{2}\left[\left(\frac{\partial \Phi}{\partial x}\right)^2 + \left(\frac{\partial \Phi}{\partial z}\right)^2\right] + \frac{p_{atm}}{\rho} + g\,z = C(t) \tag{3}$$

The resulting boundary value problem can be solved analytically giving the following velocity and pressure values:

$$u = \frac{H}{2}\sigma \frac{cosh(k(h+z))}{sinh(kh)} cos(kx - \sigma t) \tag{4}$$

$$v = \frac{H}{2}\sigma \frac{sinh(k(h+z))}{sinh(kh)} sin(kx - \sigma t) \tag{5}$$

$$p = -\rho g z + \rho g \frac{H}{2} \frac{cosh(k(h+z))}{cosh(kh)} cos(kx - \sigma t) \tag{6}$$

The function that defines a regular ocean wave is described in Equation 11, where η represents the free surface elevation of the linear wave, A is the wave amplitude (H/2), ω is the wave frequency (rad/s), and k is the wavenumber.

$$\eta\,(x,t) \;=\; A\,sin\,(\omega t \;+\; kx) \tag{7}$$

The equation that relates the wavelength with a given wave frequency is the dispersion relation, provided in Equation 12.

$$\sigma^2 = g\,k\,tanh\,(k\,h) \tag{8}$$

where $\sigma = 2\pi/T$, g is gravity, h is the water depth, and T is the average wave period.

Solving numerically for the wavenumber k, the wavelength (λ) is computed, and consequently, the wave speed (C), shown in Equations 9 and 10, respectively.

$$\lambda = 2\pi/k \quad (9)$$

$$C = \lambda/T \quad (10)$$

However, as waves approach to shore and enter shallow water, wave height and wavelength are altered by shoaling and refraction processes. The wave phase speed decreases because it is proportional to the square root of water depth, which causes then the wavelength to decrease, since the wave period remains unchanged. Additionally, the wave height increases and distance between waves decrease. Refraction is then the change of direction of the wave, and shoaling is the process by which wave height increases, both associated with the change of speed due to bathymetry (Dean & Dalrymple, 1991).

Shallow water is considered when *kh* is small, then $h \ll \lambda$, thus $\frac{\lambda}{20} < h$. Consequently, wave celerity and wavelength decrease. In shallow water, waves are nondispersive, which means that wave speed is independent of wavelength. This indicates that all waves with any wavelength will propagate at the same speed (Dean & Dalrymple, 1991).

3.2.2. Wave Spectra

By looking at the ocean surface, it can be noticed that the ocean waves move with different frequencies, phases, amplitudes, and directions. To describe a realistic approach to ocean waves, wave spectra is necessary (Dean & Dalrymple, 1991).

A propagating wave train is described in Equation 11, with the difference from linear theory that another wave train is added.

$$\eta\,(x,t) = \sum_{n=0}^{\infty} A_n \, sin\,(\omega_n\, t \, + \, kx) \quad (11)$$

The n^{th} moment of the wave spectrum is defined as

$$m_n = \int_0^{\infty} f^n \, S(f) \, df \tag{12}$$

where *f* is the frequency and *S(f)* is the spectra.

Then, the wave height and period are defined as follows (equations 13-15)

- Significant Wave Height: $H_s = 4\sqrt{m_o}$ (13)
- Mean Period: $T_m = \frac{m_0}{m_1}$ (14)
- Peak Period: $T_p = \frac{1}{f_p}$ (15)

where significant wave height (H_s or $H_{1/3}$) is the average height of the 1/3 of the sample measured waves having the greatest heights, the mean period is the reciprocal of the mean frequency of the spectrum, m_o is the variance of the wave displacement time series, and f_p is the peak frequency.

3.3. Wave Energy Calculations

As previously defined in the literature review, wave energy can be captured in various different ways; (1) using a floating system that extracts energy from the movement up and down of the ocean waves to drive a hydraulic pump or generator; (2) using an overtopping device where the waves are funneled into an elevated reservoir where the water flows out driving a turbine; (3) utilizing an oscillating water column where the motion of the waves force a column of air to drive a turbine and therefore generating electricity.

The total energy contained in a wave consists of both potential and kinetic energy. The potential energy ($\overline{PE}$) depends solely on the wave height, which is the result of the displacement of the free surface. The kinetic energy ($\overline{KE}$) is the resulting of the movement of the water particles. The average potential and kinetic energy per unit surface area (in J/m^2) are calculated using Equations 16 and 17, respectively. Both equations are obtained by integrating over a wavelength (Dean & Dalrymple, 1991).

$$\overline{PE} = \frac{1}{16}\,\rho\, g\, {H_s}^2 \tag{16}$$

$$\overline{KE} = \frac{1}{16}\,\rho\, g\, {H_s}^2 \tag{17}$$

Consequently, the total energy per unit surface area is calculated:

$$E = \overline{KE} + \overline{PE} = \frac{1}{8}\,\rho\, g\, {H_s}^2 \tag{18}$$

Where ρ is the density of seawater (1030 kg/m^3) and H_s is the significant wave height.

This work focuses on the heave motion of the device, therefore only the potential energy of the waves would be captured. The theoretical energy potential per unit surface area for this model is calculated using Equation 19.

$$E = \overline{PE} = \frac{1}{16}\,\rho\, g\, {H_s}^2 \tag{19}$$

Additionally, ocean waves transmit energy as they propagate. The rate at which this energy is transferred is called the energy flux (*P).* The average energy flux per unit width is obtained by averaging over a wave period and integrating up to the mean free surface (*η),* and it is shown in Equation 20, where *P* represents the energy flux per meter of the wave crest (W/m).

$$P = EC_g \tag{20}$$

Where E is the average energy per unit area, and C_g is the group velocity defined in Equations 21 and 22.

$$C_g = nC \tag{21}$$

$$n = \frac{1}{2}\left(1 + \frac{2kh}{tanh(kh)}\right) \tag{22}$$

The concept of group velocity was derived in terms of the rate at which a train of propagating waves is transferring energy. It was originated by superimposing trains of waves at different frequencies and wavenumbers and results in an envelope that propagates with speed C_g (Dean & Dalrymple, 1991). The characteristics of a wave train is shown in Figure 13.

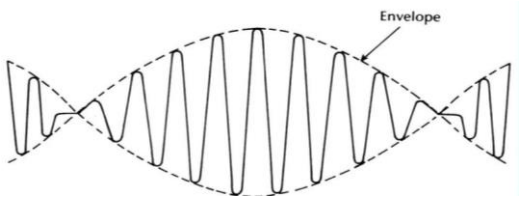

Figure 13. Characteristics of a wave train (Dean & Dalrymple, 1991)

In shallow water, waves are nondispersive, and therefore n is equal to 1. This means that the phase velocity (C) is equal to the group velocity (C_g), and can be computed using equation 23 (Dean & Dalrymple, 1991).

$$C = C_g = \sqrt{g\,h} \tag{23}$$

Consequently, the maximum wave power density or energy flux in shallow water can be approximated as follows (Equation 24):

$$P_{max} = E\,C_g = \frac{1}{16}\,\rho\,g\,{H_s}^2\,\sqrt{gh} = \frac{1}{16}\,\rho g^{3/2}\,h^{1/2}{H_s}^2 \tag{24}$$

As a result, greater wave power potential is obtained when the significant wave height is greater. The following section evaluates the wave characteristics at the selected location, with the ultimate goal of estimating the wave energy potential at that site.

3.3.1 Case Study: Fernandina Beach, FL

As previously mentioned, the first step of this work was to examine wave and climate conditions at the desired location. This is performed by obtaining historical data from the National Oceanic and Atmospheric Administration (NOAA) and using MATLAB to process the data. For this study, a local station off the coast of Fernandina Beach, Florida, is selected. This station is located at a water depth of 15 meters, and all obtained data is measured in time intervals of 20 minutes. The first objective is to evaluate the wave energy potential at this location on a yearly basis, and to analyze the energy density fluctuations between the different months. This is performed by evaluating recorded data from 2017 until 2019 so that all parameters are analyzed in a three-year interval. Next, significant wave height and wave period are analyzed in order to estimate the wave power potential. The parameters considered for this work are:

- Significant Wave Height: H_s or $H_{1/3}$
- Dominant Wave Period: DPD or T_p
- Average Wave Period: APD or T_m

The dominant wave period (DPD) corresponds to the wave period with the highest energy at a specific point, and the average wave period (APD) is the mean or average period of all waves during the 20 min interval.

Yearly histograms of both significant wave height and wave period from 2017 to 2019 are provided in Figures 14 – 15, respectively, so variations between the different seasons can be observed.

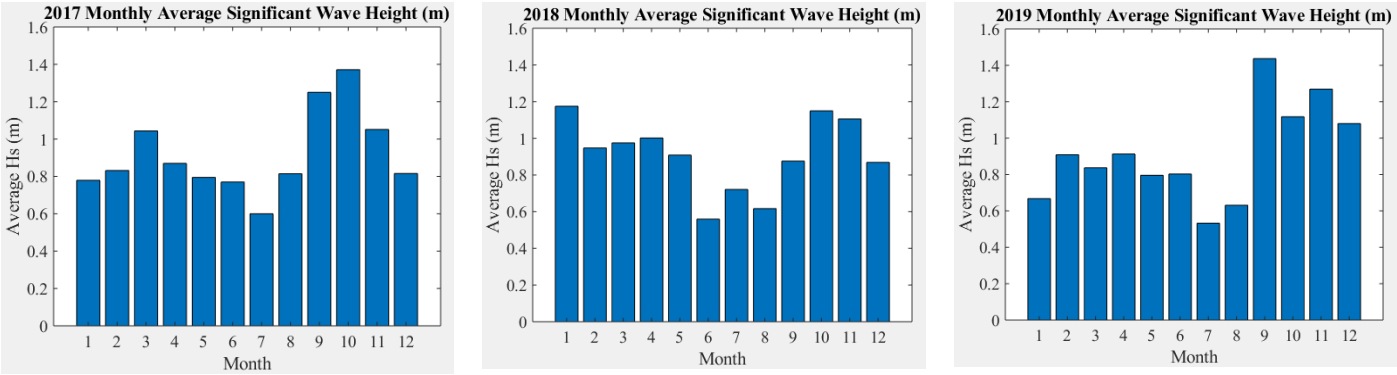

Figure 14. Yearly Histogram of Significant Wave Height (m) at Fernandina Beach 2017 – 2019

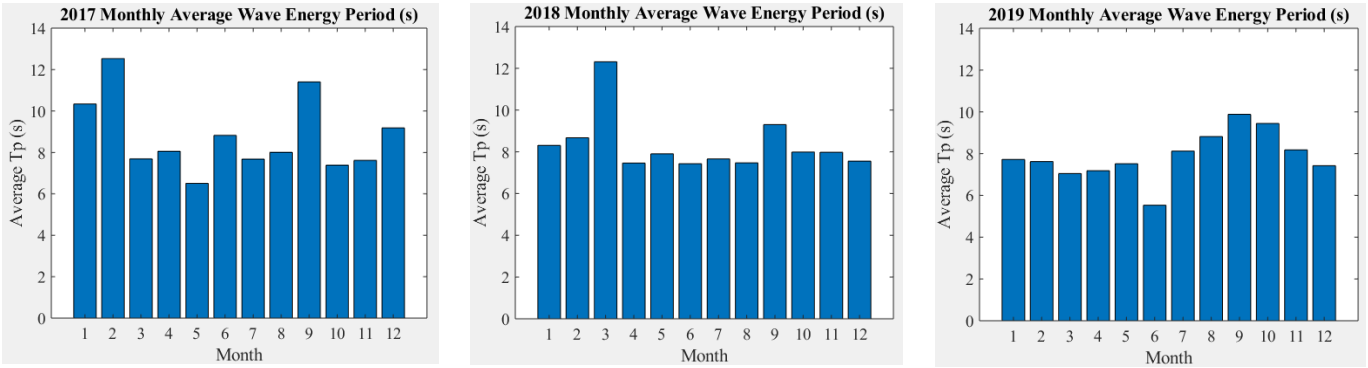

Figure 15. Yearly Histogram of Wave Energy Period (s) at Fernandina Beach 2017 – 2019

It can be determined that the significant wave height does fluctuate between seasons, as predicted. During the summer season, mostly June, July, and August, the significant wave height presents its lower values of the year, varying in the range from 0.5 to 0.8 meters. During the winter season, the significant wave height reaches its maximum values between September and December, with peaks between 1.2 – 1.5 meters height. On the other hand, the wave period

remains quite constant during most of the year with an average energy period of 8.3 seconds, reaching peaks of over 12 seconds about one month of the year. A scatter diagram of the monthly average of the significant wave height and wave period is illustrated in Figure 16, where it can be observed the more likely range of occurrence is between 7-10 seconds wave period, and 0.5-1.2 meters significant wave height.

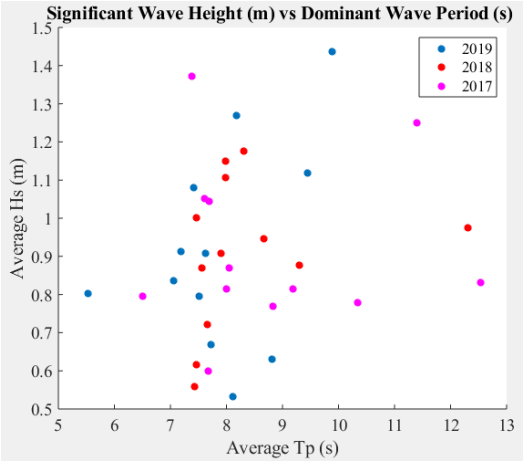

Figure 16. Scatter Diagram of the Average Significant Wave Height (m) and Wave Period (s)

Additionally, a scatter diagram of the significant wave height and dominant wave period between June and December of 2019 is presented below in Figure 17, for a comparison between the two different months. It can be observed that both the wave height and wave period present small values during the summer months, as compared to the winter months, in this case, December. As a result, both the theoretical available power and the maximum power generation are obtained during the winter time.

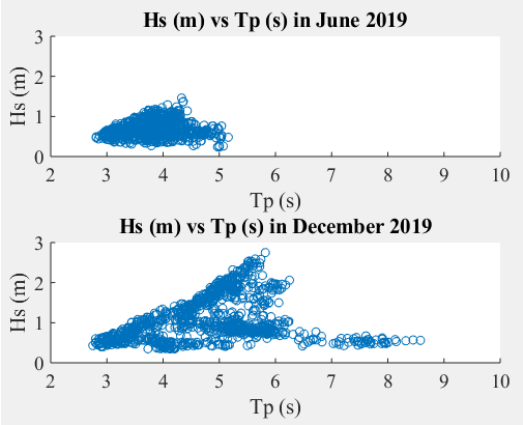

Figure 17. Scatter Diagram Comparison of Significant Wave Height (m) and Wave Period (s)

In shallow water, however, the average energy density and the maximum power potential are independent of wave period, and depend exclusively on the significant wave height, as previously shown in Equations 19 and 24, respectively. The graphs for the average energy density for the past three years, as well as the maximum theoretical power potential, are provided in Figures 18 and 19, respectively.

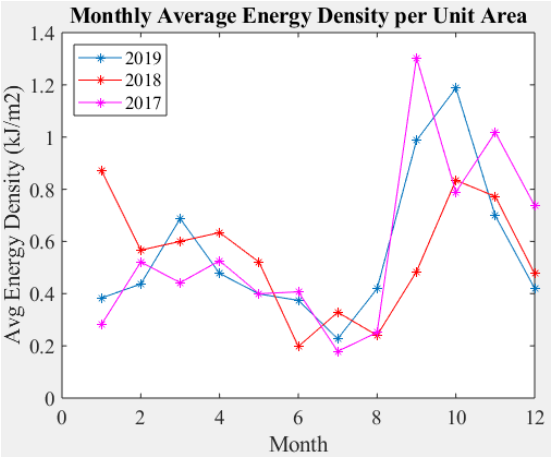

Figure 18. Monthly Average Energy Density (kJ/m^2) at Fernandina Beach

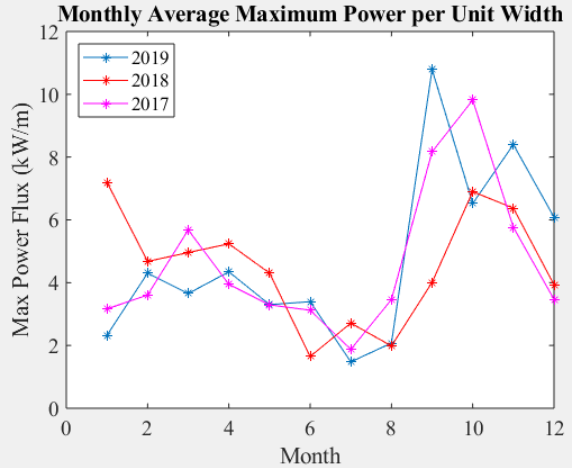

Figure 19. Monthly Maximum Theoretical Power (kW/m) at Fernandina Beach

Additionally, the obtained results for the energy flux per unit width at this site are provided in Table 2.

Table 2. Maximum theoretical wave power (W/m) at Fernandina Beach

Hs (m)	Period (s)							
	3.0	4.0	5.0	6.0	7.0	8.0	9.0	10.0
0.25	92	123	154	185	216	247	277	308
0.50	370	493	616	740	863	986	1,109	1,233
0.75	832	1,109	1,387	1,664	1,941	2,219	2,496	2,773
1.00	1,479	1,972	2,465	2,958	3,451	3,944	4,437	4,930
1.25	2,311	3,081	3,852	4,622	5,392	6,163	6,933	7,703
1.50	3,328	4,437	5,546	6,656	7,765	8,874	9,983	11,093
1.75	4,529	6,039	7,549	9,059	10,569	12,079	13,589	15,098
2.00	5,916	7,888	9,860	11,832	13,804	15,776	17,748	19,720
2.25	7,487	9,983	12,479	14,975	17,471	19,966	22,462	24,958
2.50	9,244	12,325	15,406	18,487	21,569	24,650	27,731	30,812
2.75	11,185	14,913	18,642	22,370	26,098	29,826	33,555	37,283
3.00	13,311	17,748	22,185	26,622	31,059	35,496	39,933	44,370

Lastly, the spectral density at that station computed by the NOAA is shown in Figure 20.

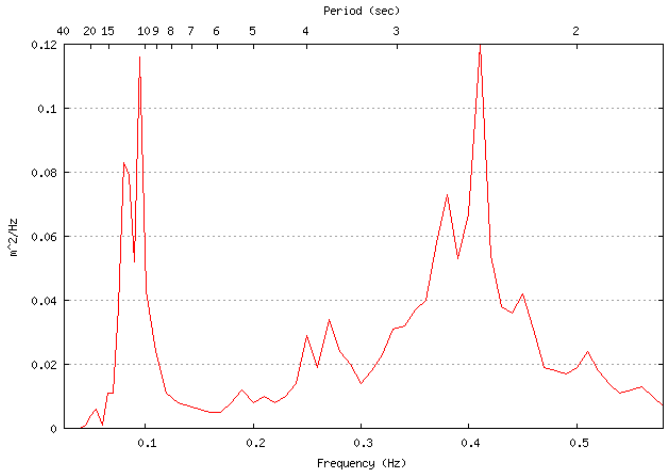

Figure 20. Spectral Density at Fernandina Beach (Station 41112) on 04/09/2020

4. Proposed System

The hypothesis that initially drove this research was that system of pulleys and counterweights coupled together, working like a “yo-yo” system, could be an efficient system to harness energy from waves to produce electric power, with little initial investment, and low maintenance. The system would be composed of a system of pulleys enclosed inside a floating buoy, and ultimately connected to a generator to produce electricity from the heave motion of the device. One of the challenges of this system was to design a counterweight system so that the pulleys can rotate back and forth as the buoy moves up and down. Another challenge was, and most importantly, that the generator will need to be enclosed in another structure so that the relative motion of the buoy with respect to the energy storage system could be achieved. This, added to the complication of the mooring of such devices, led us to discard this model and look for another alternative.

The new proposed design arose with the idea of something as simple as an induction flashlight, which produces electricity by simply shaking the flashlight along its long axis, causing a magnet to slide through a coil of wire. Faraday's law of induction states that a changing magnetic field generates an electric current in a conductor and vice versa. This principle could be applied to a device floating over the ocean's surface and using the upward and downward motion of the waves to slide a magnet through a coil of wire.

The system would be composed of a hollow cylinder structure where the permanent magnet is enclosed, with a top and bottom clearance that allows the vertical motion of the magnet. Then, the coil of wire would be looped around the structure and hold in place by two exterior rings. The 3D model of the proposed configuration is illustrated in Figure 21.

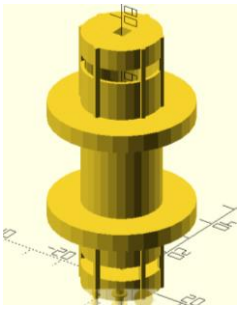

Figure 21. 3D Model of the proposed design

However, this proposed design presented some limitations. One of the challenges is to restrict the device motion so that the structure moves exclusively in the vertical direction, and does not bend over to the sides as the waves hit the device. This could be achieved by mooring the structure with four mooring connection lines. The mooring configuration would need to be stiff enough to restrict the body from moving horizontally, and therefore dissipating wave energy, but allowing it to move in the vertical position.

A modification of this proposed design is then considered. The coil structure could be submerged underwater in a hollow cylinder fixed to the seabed. Then, the permanent magnet would also be submerged and attached to a floating body on the surface, allowing the magnet to freely move up and down inside the structure with the motion of the waves. A sketch of the proposed modification with two different floating bodies is presented in Figure 22, where the coil structure is marked in red, the permanent magnet is dark gray and attached to the floating body, marked in yellow.

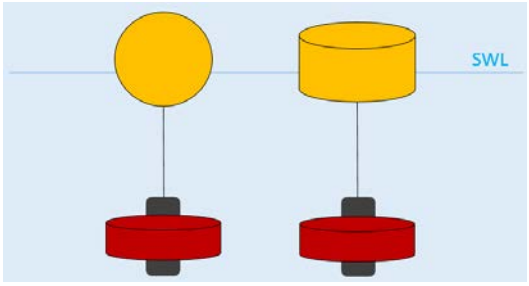

Figure 22. 3D Model of the proposed modified design

Then, the different types of magnets that would be more suitable for this work are evaluated. There are several types of magnet compositions depending on their application. Some of the most widely used permanent magnets in marine applications are samarium-cobalt magnets, due to their high resistance to corrosion. However, about 20 years after these were discovered, a more powerful type of rare earth magnet was invented. Neodymium magnets were developed in the 1980s by General Motors and Sumitomo Special Metals, by combining neodymium with small amounts of iron and boron. These can create magnetic fields of up to 1.4 T (Tesla), compared to the 0.5 – 1 T from samarium-cobalt, alnicos (aluminum-nickel-cobalt) or ceramic magnets. Neodymium magnets are an alloy of about 65% iron content, 30% neodymium, and 5%

boron ($Nd_2Fe_{14}B$). A comparison of the physical properties between samarium-cobalt and neodymium magnets is presented in Table 3.

Table 3. Comparison of the physical properties for different types of magnets

Property	Symbol	$Nd_2Fe_{14}B$	$SmCo_5$	Sm_2Co_{17}
Density (kg/m3)	ρ	7,500	8,200 – 8,400	8,300 – 8,500
Vickers Hardness (DPN)	Hv	570	500-600	450 - 500
Compression Strength (N/mm2)	CS	780	9,000-1,000	650 - 800
Electrical resistivity (μ Ω.m)	r	1.5	0.05 – 0.06	0.8 – 0.9
Electrical conductivity (10^6 S/m)	s	0.667	17 – 20	1.11 – 1.25
Thermal conductivity Cal/(m.h.°C)	k	7.7	11	10
Specific Heat Capacity (kcal/kg °C)	C_p	0.12	0.08	0.09
Youngs Modulus (10^{11}N/m^2)	L/E	1.6	1.6	1.2
Poissons ratio	v	0.24	0.27	0.27
Rigidity (N/m2)	$E \times L$	0.64	150	150

As a result, a neodymium magnet is suggested as the most powerful and most suitable for this work. A set of four neodymium permanent magnets and two coils of wire are purchased to assemble a small-scale model of the proposed prototype. The magnetic force of the permanent magnet is 0.5 Tesla, and they each have 12 disks of 32 mm diameter and a height of 3 mm high each, giving a total height of 36 mm.

Next, the main concepts for this design are evaluated in the following section.

5. Design Concepts

5.1. Degrees of Freedom

A floating body has six degrees of freedom, three rotational and three translational, which are shown below in Figure 23. The translational motion in the *X, Y*, and *Z* coordinates are surge, sway, and heave, respectively. The rotational motion around the *X, Y*, and *Z* axes are roll, pitch, and yaw, respectively.

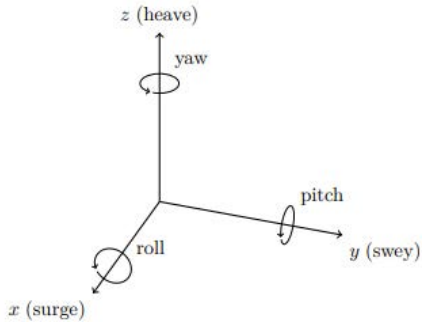

Figure 23. Degrees of freedom of a floating body (ANSYS AQWA)

For this work, the focus is to limit the motion of the device exclusively to the heave mode, so that the maximum efficiency of the system can be achieved. Therefore, if only the vertical direction is considered for a single frequency wave fluctuation, Equation 7 to define a linear wave can be simplified as follows:

$$x = A \sin(\omega t) \tag{25}$$

Then, the hydrostatic and hydrodynamic forces acting on the floating system are analyzed.

5.2. Forces Acting on the System

5.2.1. Hydrostatic Forces

Recalling Archimedes' Principle, the buoyant force of the device must be equal to the weight of the fluid displaced. The weight of the object is calculated using Equation 26. Consequently, the buoyancy force (F_b) which is the resultant of all hydrostatic forces over the wetted surface, is computed using Equation 27, and the uplifting force or hydrostatic pressure acting on the body is computed in Equation 28.

$$W = m\,g \tag{26}$$

$$F_b = -\rho\,g\,\forall(t) \tag{27}$$

$$F_u = -\rho\,g\,Z_o(t) \tag{28}$$

where m is the mass of the structure (kg), ρ is the density of seawater (1030 kg/m^3), $\forall$ is the displaced volume (m^3), and Z_o is the wetted height of the body (m), or distance from the bottom of the device to the SWL. The mass of the structure is computed as follows:

$$M = \rho d\,\forall = \rho d\,\pi\,\frac{D^2}{4}\,hd \tag{29}$$

where ρ_d is the density of the body (kg/m^3), D is the diameter of each device (m), and h_d is the height of the structure (m).

For static equilibrium in calm water level, all forces must be balanced (Archimedes' Principle). This is shown in Equation 30.

$$W - Fb - Fu = 0 \tag{30}$$

Additionally, for a body in heave mode, the force on the system can be obtained from the linearized pressure, which is computed using the Bernoulli Equation, shown in equation 31. The net pressure force is then computed using Equation 32, which for hydrostatic conditions will always be pointing upward.

$$\frac{P}{\rho} + \frac{\partial \Phi}{\partial t} + \frac{1}{2}\left[(u)^2 + (w)^2\right] + g\,\eta = 0 \tag{31}$$

$$F = \int P\, dA \tag{32}$$

For maximum efficiency of the device, the floating system must be in resonance with respect to the dominant incident waves. This means that maximum energy extraction occurs when the system is oscillating with a frequency similar or very close to the incoming wave's natural frequency (Mei 1976). The undamped natural frequency (ω) of the system is calculated in Equation 33, and the natural frequency (ω_n) of the incident waves is shown in Equation 34.

$$\omega = \sqrt{\frac{\rho\, g\, A}{M}} \tag{33}$$

$$\omega_n = \frac{1}{T_p} \tag{34}$$

where A is the water surface area of the body, and $M = m + m_a$, where m is the system's total mass and m_a is the total added mass.

5.2.2. Hydrodynamic Forces

For linear wave theory, the total wave force can be calculated as a sum of drag force and inertia force, which both propagate continuously in a wave field (Morison et al. 1950). The Morison equation for the total force is provided in Equation 35.

$$dF = dF_D + dF_I = \frac{1}{2} C_d \rho A u |u| + C_M \rho \Omega \frac{Du}{Dt} \quad (35)$$

where C_D and C_I are the drag and inertia coefficients, respectively.

For constant values C_D and C_I, and simplifying for heave mode only, linear wave theory is used to solve for the total force, as shown in Equation 36.

$$F = C_d D n E \sin^2(\sigma t) + C_M \pi E \frac{D^2}{H} \tanh(k h) \cos^2(\sigma t) \quad (36)$$

In addition, basic theory in AQWA states that wave forces acting on diffracting structures can be modeled using the Morison Equation, neglecting viscous effects. For cylindrical elements whose diameter is relatively small compared to wavelength ($D/\lambda < 0.2$), the hydrodynamic force per unit length (Newton) is calculated using the Morison Equation. This is shown in Equations 37 and 38, and the forces that sum the total hydrodynamic force are the following:

- Froude-Krylov Force: from the pressure in the undisturbed waves
- Diffraction Force: due to a stationary structure disturbing the incident waves
- Radiation Force: due to the oscillation of the structure, generating waves
- Drift Force: net force due to high order effect

$$F = F_{FK} + F_I - F_R + F_D \quad (37)$$

$$F = \rho \Omega a_w + \rho C_a \Omega a_w - \rho C_a \Omega \ddot{X} + \frac{1}{2} \rho C_d D U |U| \quad (38)$$

where Ω is the volume of the element per unit length (m^3/m), a_w is the acceleration of the flow (m/s^2), $\ddot{X}$ is the acceleration of the body (m/s^2), and U is the relative velocity between the flow and the body (m/s). C_a and C_d are the added mass and drag coefficients, respectively, and can also be combined in terms of the inertia coefficient.

$$C_I = 1 + C_a \tag{39}$$

The response X of the structure is obtained by solving the motion equation in the frequency domain, shown in Equation 40 (ANSYS AQWA).

$$F(\omega) = M_s \ddot{X} + M_a(\omega) \ddot{X} - B(\omega) \ddot{X} + C \ddot{X} \tag{40}$$

where F is the wave excitation force, M_s is the mass structure, Ma is the added mass, B is damping, and C is hydrostatic stiffness.

5.3. Electromagnetic Induction Calculations

Faraday's Law of Induction describes how an electric current produces a magnetic field (MF) and, conversely, how a changing magnetic field induces an electric current in a conductor generating an electric field (EF). The importance of this discovery was tremendous. Electromagnetic induction allowed the development of electric motors, generators, and transformers, which is the reason why we currently have access to an electric power grid (Faraday 1831).

The electromagnetic induction principle can then be applied to generate an electric current by generating a magnetic field from the motion of ocean waves. A magnetic field is represented by magnetic flux lines, as illustrated in Figure 24.

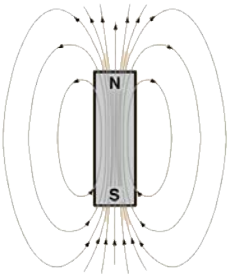

Figure 24. Flux lines of a permanent magnet's magnetic field (Journal of Applied Physics)

The current induced (*I*) and the voltage generated (*V*) by a magnetic field is calculated as shown in Equations 41 and 42, respectively.

$$I = \frac{2\,\pi\,r\,B}{\mu o} \tag{41}$$

$$V = -\,N\frac{B*A}{t} \tag{42}$$

where *B* is the magnetic field, *r* is the distance, and μ_o is the magnetic permeability of free space ($\mu_o = 4\pi*10^{-7}$ Newton/Ampere^2 or Henry/meter), *N* is the number of coils, *A* is the cross-sectional area of the coil, and *t* is the time that it takes the magnet to go through the coil one way, therefore it is half of the wave period ($t = Tp/2$).

Then, the maximum power captured (P) is computed using the general formula shown in Equation 43.

$$\mathrm{P} = \mathrm{V} \times \mathrm{I} = \frac{\mathrm{N\,B}\,\frac{\pi}{4}\,\mathrm{D}^2}{\mathrm{T}_p/2} \times \frac{2\,\pi\,\frac{\mathrm{D}}{2}\,\mathrm{B}}{\mu\mathrm{o}} = \frac{\mathrm{N}\,\pi^2\,\mathrm{B}^2\,\mathrm{D}^3}{4\,\mathrm{T}_p\,\mu\mathrm{o}} \tag{43}$$

In the next section, the modeling approach for the proposed system is presented.

6. Modeling Approach

To analyze and study the model interaction with the working environment, ANSYS software, and particularly the AQWA module, was used. Since a final design of a prototype has not been decided yet, this analysis intends to evaluate two different body shapes, from the initial idea presented previously in Section 4. The objective of this approach is to verify the AQWA results with experimental results, that will be part of the future work of this research, in order to conclude with a model for the final design. Additionally, both simulations are run at two different water depths of 3 and 15 meters, to compare results.

The purpose of these simulations was based on the idea of having a floating body that moves in the heave mode with the motion of the waves, attached to a permanent magnet submerged under water, and inducing the current of a fixed coil as the permanent magnet moves up and down with the floating device. The goal is then to analyze and compare the two different shapes and determine which one would be more suitable for the proposed model.

The shapes analyzed are a cylinder and a sphere. Both bodies dimensions are selected so that both have the same volume (1.77 m^3). The sphere has a diameter of 1.5 meters, and the cylinder has a diameter of 1.5 meters and a height of 1 meter, although the dimensions of the final prototype have not been decided yet. Furthermore, both bodies are moored using a conventional catenary linear cable, fixed to the seabed. The evaluation of the different types of mooring configurations and materials are also included in the future steps of this work. A 3D model of both models is provided in Figure 25.

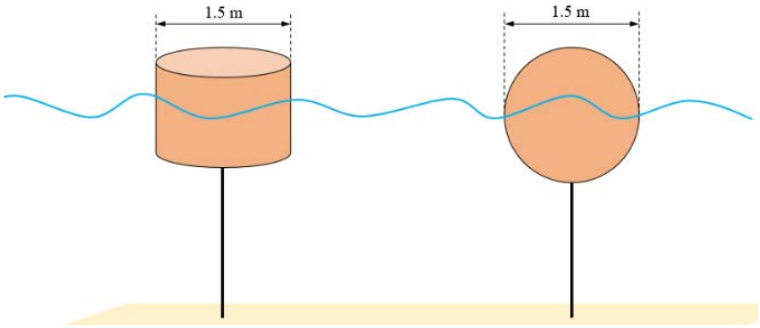

Figure 25. 3D Model of Cylinder and Sphere Models

Using AQWA, both hydrodynamic diffraction and hydrodynamic response analyses are performed. For hydrodynamic diffraction, multi-directional wave-analysis is included with wave directions varying from -180° to 180° with 45° increments. Over 2000 cells are used with a maximum element size of 0.1 m.

The hydrodynamic diffraction analysis computes all hydrodynamic forces acting on the body, and the hydrodynamic response performs static stability analysis, time response, and spectral response analysis of the model. The simulations performed on both models include: (1) hydrodynamic diffraction (2) static stability analysis, (3) time response analysis, and (4) frequency domain analysis.

- Hydrodynamic Diffraction
    - Hydrostatic Table
    - Froude – Krylov Force vs Frequency
    - Diffraction Force vs Frequency
    - Radiation Damping Force vs Frequency
- Static Stability
    - Natural Modes

- Time Response Analysis
    - Structure Position – Actual Response
    - Structure Position – RAO Based Response
    - Wave Surface Elevation
- Frequency Response Analysis
    - Wave Spectra
    - Position Response Spectra
    - Force/Moment Spectra
    - Frequency Domain Statistics

All results obtained are attached to Appendix A, B, C, and D, respectively, and the most relevant are discussed in the following section.

6.1. Results and Discussion

A) Hydrodynamic Diffraction

First, the hydrostatic table is computed, which provides hydrostatic stiffness, displacement properties, and stability parameters. Results were similar at both water depths, and this is shown in Appendix A.1.a for cylinder and Appendix A.1.b for the sphere.

The hydrodynamic forces acting on both bodies and at both different water depths are computed, including Froude-Krylov, diffraction, or also called wave inertia, and radiation damping. This analysis is performed within the range of the wave periods observed from the NOAA data, between 5 and 13 seconds. First, the analysis at 3 meters water depth is computed, and results are provided in Table 4, Furthermore, these results are illustrated graphically in the bar chart in Figures 26 and 27, respectively.

Table 4. Hydrodynamic Forces Comparison between Both Models (N/m)

	Cylinder				Sphere			
T (s)	Froude-Krylov (N/m)	Diffraction (N/m)	Radiation (N/m)	Total (N/m)	Froude-Krylov (N/m)	Diffraction (N/m)	Radiation (N/m)	Total (N/m)
13.00	795.4	396.4	0.309	1,192	793.3	410.6	0.3158	1,204
11.35	912.8	455.8	0.473	1,369	910.2	471.2	0.484	1,381
10.07	1,031	515.9	0.693	1,547	1,028	532.2	0.707	1,560
9.05	1,150	576.9	0.980	1,727	1,146	593.7	0.997	1,740
8.22	1,270	638.8	1.347	1,909	1,265	655.7	1.368	1,921
7.53	1,390	701.8	1.809	2,092	1,385	718.2	1.833	2,103
6.94	1,512	765.9	2.386	2,278	1,506	781.3	2.412	2,287
6.44	1,635	831.3	3.100	2,466	1,628	845.1	3.125	2,473
6.01	1,760	898.2	3.976	2,658	1,752	909.6	3.998	2,662
5.63	1,886	966.7	5.047	2,853	1,877	975	5.058	2,852
5.30	2,014	1,037	6.351	3,051	2,003	1,041	6.343	3,044
5.00	2,143	1,109	7.931	3,252	2,131	1,109	7.893	3,240

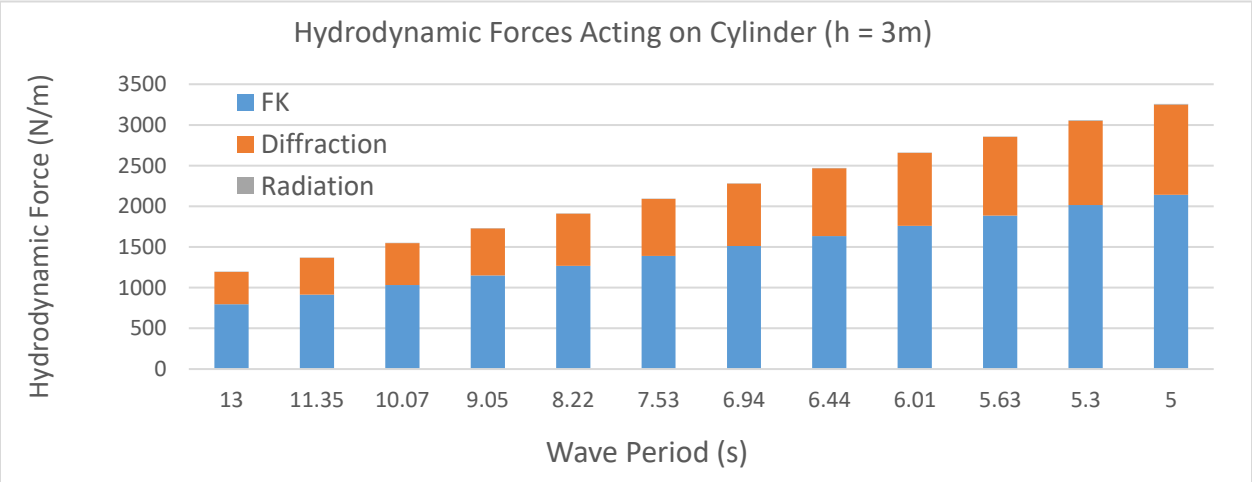

Figure 26. Hydrodynamic Forces Acting on Cylinder at h = 3 m. (N/m)

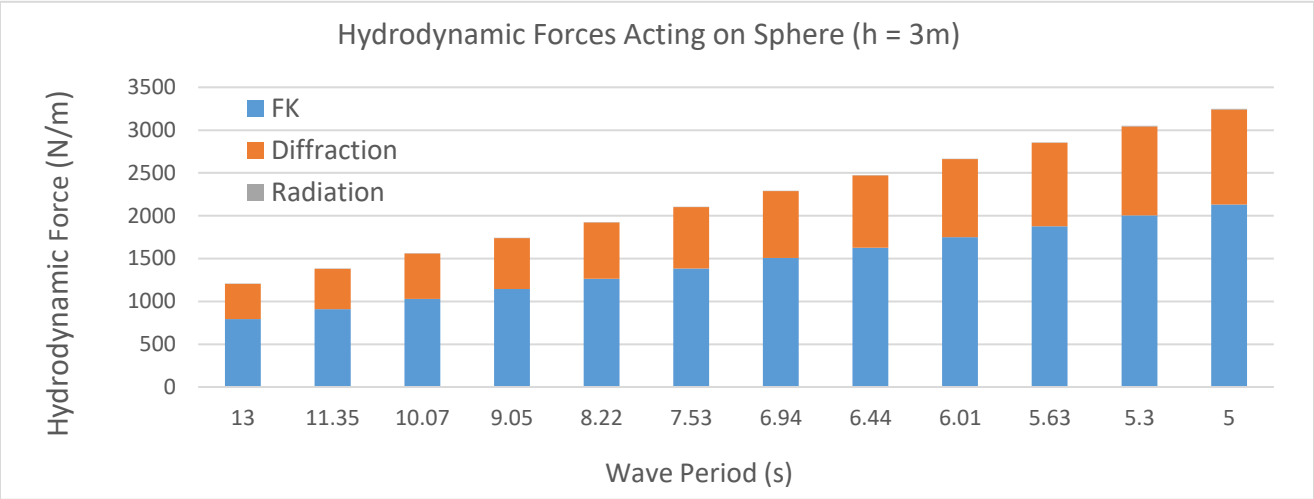

Figure 27. Hydrodynamic Forces Acting on Sphere at h = 3 m. (N/m)

It is observed that the radiation force can be neglected, so the total hydrodynamic force is computed by adding the Froude-Krylov and the diffraction forces. The hydrodynamic force acting on both models was found to be very similar. As a result, this hydrodynamic analysis does not provide a significant difference between one model or the other. The cylinder body ranges from a minimum of 1192 N/m and a maximum of 3252 N/m, and the sphere model has a force range between 1,204 N/m and 3,240 N/m. The hydrodynamic force acting on the model becomes larger as the wave period decreases.

The obtained results at 15 meters water depth are shown in Figure 28, for the sphere in this case since both models are very similar. It is observed that both Froude-Krylov and diffraction forces decrease significantly at deeper water, with the hydrodynamic force ranging from a minimum of 564 N/m to a maximum of 2,096 N/m.

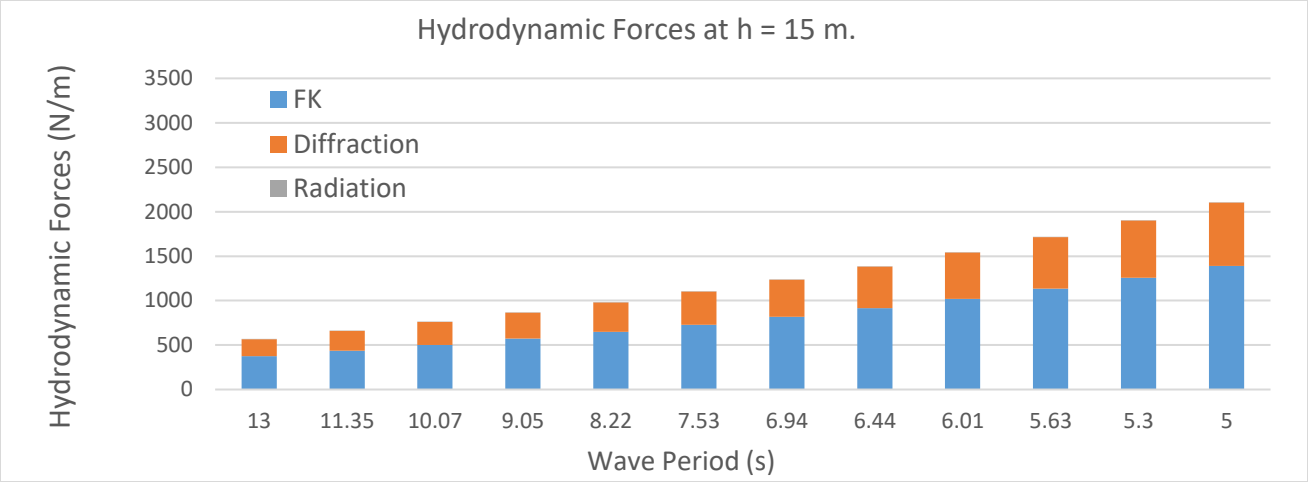

Figure 28. Hydrodynamic Forces Acting on Sphere at h = 15 m. (N/m)

Besides, the comparison of the hydrodynamic forces at 3 and 15 meters water depth, respectively, is provided in Figure 29, where the maximum is 3,240 N/m versus 2,096 N/m, and the minimum found is 1,204 N/m versus the 564 N/m.

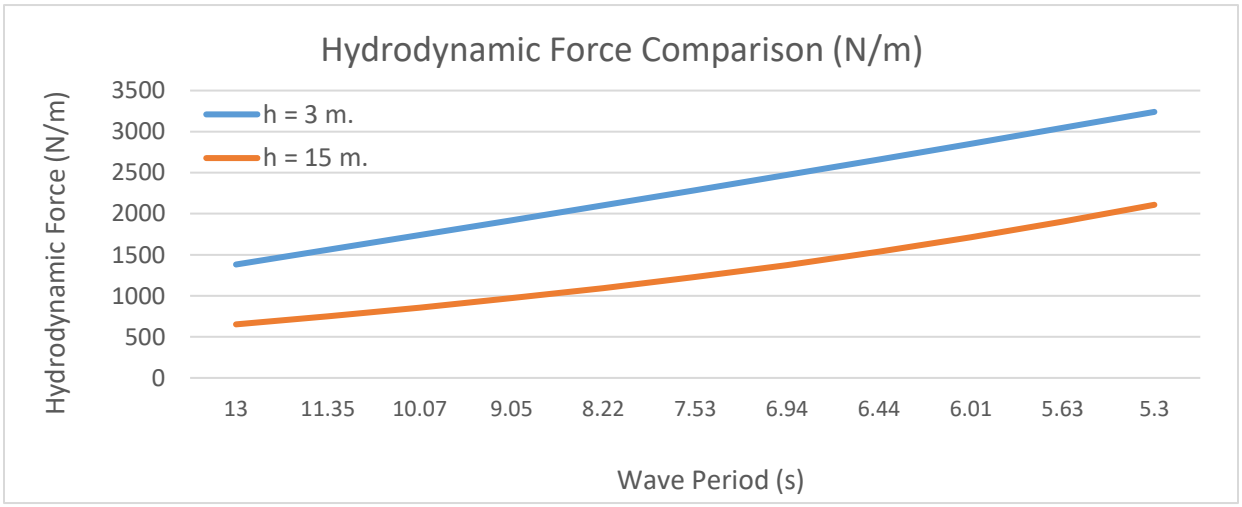

Figure 29. Hydrodynamic force comparison at different water depths (N/m)

Additionally, the hydrodynamic forces were also computed in MATLAB utilizing flow acceleration calculations obtained from the wave data, so that the simulation results can be verified. The graphical computation for both Froude-Krylov and diffraction forces using MATLAB is shown in Figure 30, and Table 5 provides a comparison between the obtained results. It can be noticed that the computed forces using MATLAB are very similar for both models.

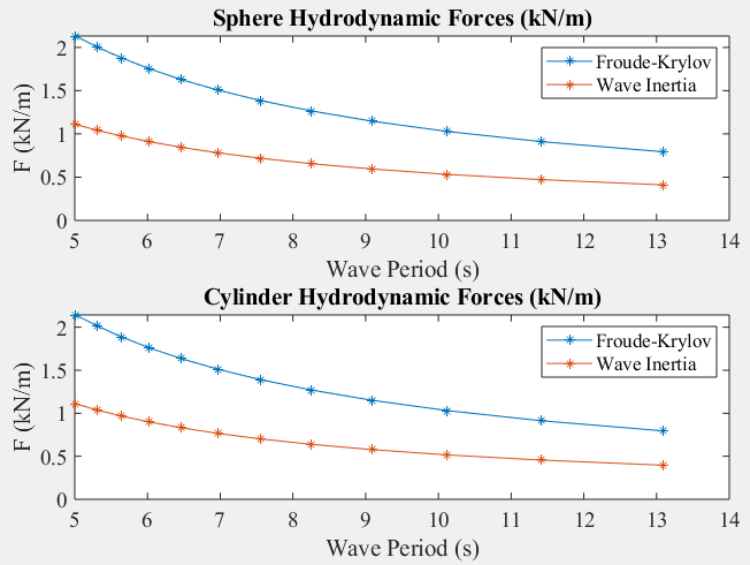

Figure 30. Froude-Krylov and Wave Inertia Forces on Each Model (kN/m)

Table 5. Hydrodynamic Froude-Krylov Force Comparison

Wave Period (s)	MATLAB (N/m)	Cylinder (N/m)	Sphere (N/m)
13.00	871	795.4	793.3
11.35	998	912.8	910.2
10.07	1,126	1,031	1,028
9.05	1,253	1,150	1,146
8.22	1,381	1,270	1,265

7.53	1,508	1,390	1,385
6.94	1,636	1,512	1,506
6.44	1,763	1,635	1,628
6.01	1,891	1,760	1,752
5.63	2,018	1,886	1,877
5.30	2,146	2,014	2,003
5.00	2,273	2,143	2,131

The results computed in MATLAB are found to be similar to the results obtained using AQWA, with a slightly over-prediction in MATLAB computations, or slightly under-prediction using AQWA software. Furthermore, the Force/Moment vs Frequency graph computed from all hydrodynamic forces is provided in Appendix A1, including (1) Froude – Krylov (2) diffraction, and (3) radiation damping.

B) Static Stability Analysis

The static stability analysis computes the natural modes of the model, and determines whether the system is stable or not. For this simulation, two natural modes are found on each model, both being stable. The natural modes are attached to Appendix B1.

C) Time Response Analysis

The time response analysis was run with a regular incident wave, using the average wave period and wave amplitude from the data (0.91 meters wave height, and 8.3 seconds wave period). The structure position with respect to time for each model is computed using the

Response Amplitude Operator (RAO). Since both models are very similar, the frequency of the heave motion is consistent with the period of incoming waves, as shown in Figure 31.

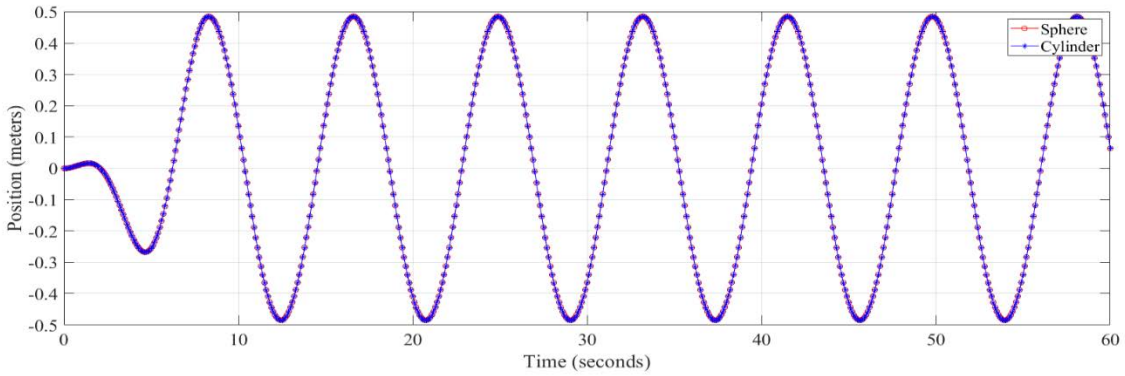

Figure 31. Structure Position (RAO-Based Response) – Global Z

D) Frequency Response Analysis

The frequency analysis is computed using a Pierson-Moskowitz spectrum. The wave spectrum parameters are set to be the data average, so the significant wave height is set to 0.9 meters and the zero-crossing wave period to 8.3 seconds. The analysis presented similar results for both water depths, so only the wave spectra obtained at 3 meters for each model are presented below in Figures 30 and 31. The obtained results at 15 meters are attached to appendix D.

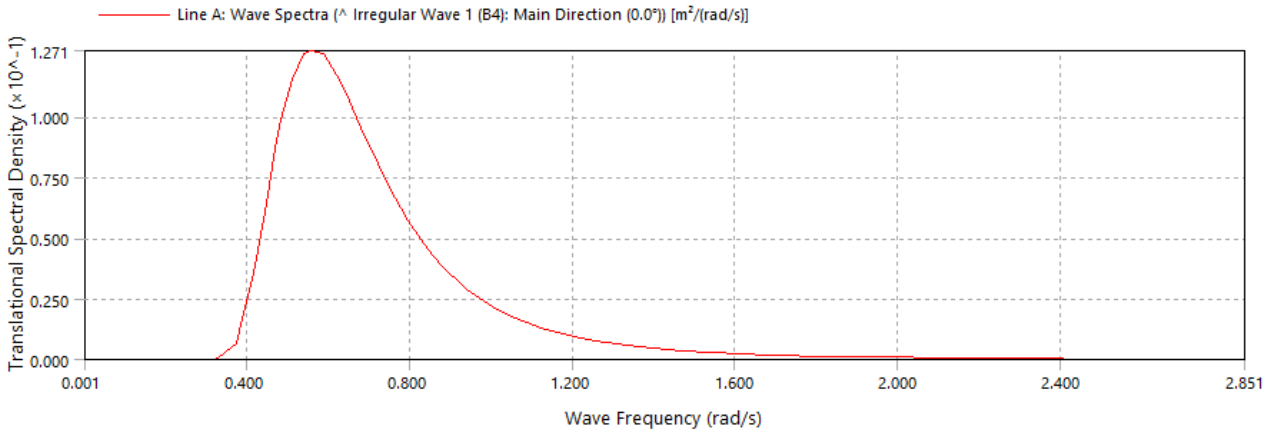

Figure 32. Cylinder Wave Spectra

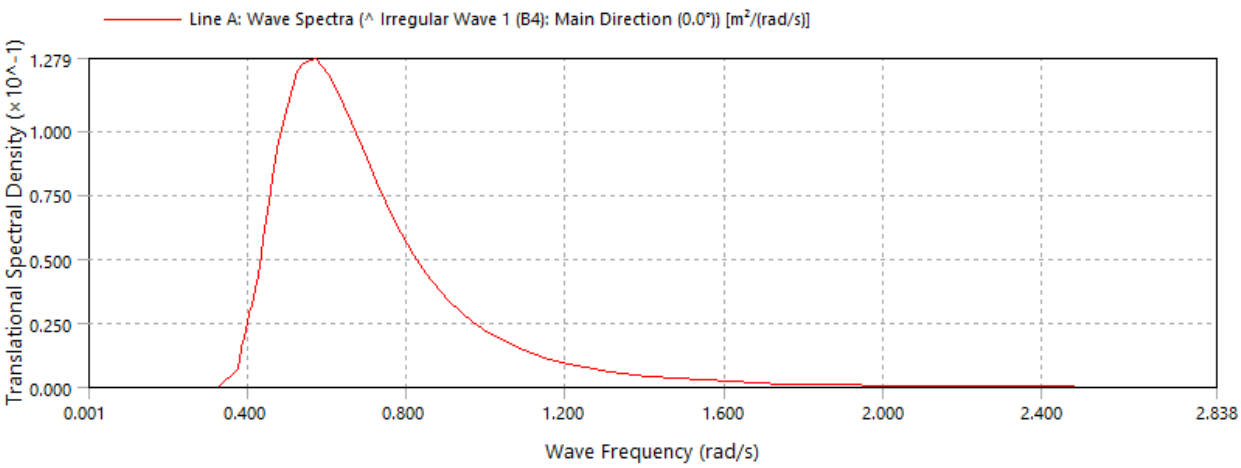

Figure 33. Sphere Wave Spectra

In addition, position response spectra, force/moment spectra, and frequency domain statistics are also computed and shown in Appendix D.

Next, the environmental impacts of electromagnetic fields are evaluated.

7. Environmental Impacts of Electromagnetic Fields

According to the World Health Organization (WHO), electric and magnetic fields are generated by natural phenomena. The atmosphere has a radially directed electric field with an average strength of around 100 V/m, although it can range from 50–500 V/m depending on weather, latitude, time of the day and season. During bad weather or thunderstorms, the values can reach up to ± 40 000 V/m (König et al., 1981 as cited in IARC, 2002). Also, the Earth has a natural geomagnetic field that varies over the surface between 30 - 70 μT (10^{-6} Tesla), reaching their maxima at the poles, and their minimum at the equator. Previous research estimates that the average person exposure to EMF can vary from 0 to 0.68 μT, daily (Lacy-Hulbert et al. 1998; Preece et al. 2000; Kheifets et al. 2005 as cited in McNamee et al., 2009. However, anything

below the Earth's natural field can be considered insignificant and will not affect human life (WHO, 2016).

The smallest magnetic field that has been proved to trigger a human response is in the range of 10,000 - 20,000 μT (0.01 -0.02 T) (Legros, 2018). Although this threshold is well above the strength of any magnetic field encountered in everyday life, to produce an impact in human beings the field must be time-varying. Alternating magnetic fields are those that change intensity and direction over time and are usually expressed in T/s. These can induce an electric current in the body, creating numerous adverse health effects. On the other hand, static magnetic fields are those that do not vary in intensity or direction over time and have a frequency of 0 Hz (Schaap et al. 2014).

Although environmental exposure to electromagnetic fields is not a new event, the growth of new technologies entails a larger presence of electromagnetic fields worldwide. Recent technological innovations are continuously increasing the strength of their electromagnetic fields, reaching values of up to 10 T, or 100,000 times stronger than the Earth's natural field (WHO, 2006). For instance, in the medical industry, an MRI scanner produces a magnetic field of around 3 T. However, these do not exert any noticeable effect on the body since the magnetic field they generate is static. According to scientist and medical biophysicist Legros, this would change if the patient inside the scanner were to rapidly move back and forth, inducing an alternating field (Legros, 2018).

The effects of electromagnetic fields depend on different factors, including field strength, the direction of the field, and the amount of time of exposure. Some of the symptoms associated with the presence of an electromagnetic field include the sensation of vertigo and nausea. International standards for public exposure to magnetic fields set an upper limit of 0.04 T for the

general public, although this can vary for pregnant women, ferrous implants, etc. For occupational exposure, the recommended limit is an average of 0.2 T, with maximum peaks of up to 2 T (WHO, 2016).

Moreover, electromagnetic fields can also influence the physical and chemical properties of water and marine life. Numerous experiments have demonstrated that water can be magnetized when exposed to a magnetic field, disturbing many properties of water, such as electromagnetism, mechanics, optics, and thermodynamics (Xiao-Feng & Deng Bo, 2008). Magnetized water (MW) has extensive utilization in agriculture, industry, construction, and medicine. It can purify wastewater, promote plan growth, inhibit the scaling of metallic surfaces, eliminate the dirt in industrial boilers, improve the performance of concrete, and aid in the digestion of food, between many other applications (Wang et al. 2018).

To obtain a better understanding of the effects of a magnetic field in water and marine life, several previous experiments of magnetic field effects are examined. Some of the most relevant include; (1) Holysz et al. examined the effect of a static magnetic field on water using frictional experiments that suggested that surface tension of magnetized water decreases, and conductivity could be enhanced (Holysz et al., 2007). (2) Cai et al. determined that the magnetic treatment decreased the intramolecular energy of water, increased the activation energy, and enlarged the mean size of water clusters. They also concluded that surface tension decreased, and more hydrogen bonds were formed by magnetic treatment (Cai et al., 2009). Later on, (3) Wang et al. likewise concluded that friction coefficient decreased with the presence of a MF, and became lower with the increase in magnetic intensity (Wang et al., 2013).

In addition, research done by Oregon Wave Energy Trust identifies the sensitivity of various marine species to electromagnetic fields (EMF). The most sensitive species to EMFs are

sharks and skates. They are known to have extreme sensitivity to low-frequency AC electric fields, especially in the range between 1/8th to 8 Hz. The next species are teleost fish, which have a lower order of magnitude than sharks. The most severe sensitivity to electric fields is found in an elasmobranch, with levels as low as 1 nV/m (10^{-9} V/m) (Fisher & Slater, 2010).

8. Economic Analysis

The elevated capital cost of wave energy systems is the main challenge that is delaying the development of wave power technologies. Plant design, construction, and power take-off costs are still relatively high, and maintenance and operation costs are still uncertain.

The method used for comparing different energy technologies and assessing its economic feasibility is the levelized cost of electricity (LCOE). The LCOE is a measure of the revenue per unit of electricity production ($/kWh) required to break even with respect to project capital and operating expenses, satisfying a minimum rate of return over the project's lifetime (EIA, 2019). It can be defined as the net present value of the electricity cost over the lifetime of the system. The average estimated LCOE of electricity of fossil fuels is in the range of 4–15¢/kWh, and the LCOE breakdown for renewable resources is provided in Table 6 (IRENA 2019).

Table 6. Global Electricity Cost in 2018 (IRENA, 2019)

Resource	5th and 95th Percentiles	Global Weighted Average
Bioenergy	4.8–24¢/kWh	6.2 ¢/kWh
Hydroelectric	3–13.6¢/kWh	4.7 ¢/kWh
Onshore Wind	4.4–10¢/kWh	5.6 ¢/kWh
Solar Photovoltaic	5.8-22¢/kWh	8.5 ¢/kWh

Concentrating Solar	11-27¢/kWh	18.5 ¢/kWh
Geothermal	6–14¢/kWh	7.2 ¢/kWh
Offshore Wind	10–20¢/kWh	12.7 ¢/kWh

Although renewable resources are still costly, IRENA estimates that offshore wind and concentrating solar power could drop to $0.06-$0.10/kWh by 2020-2022, and onshore wind and solar PV projects could consistently supply electricity for $0.03-0.04/kWh (IRENA, 2018).

Several studies among European marine projects performed by IRENA, estimated a LCOE of current tidal technologies in the range of EUR 0.17–0.23/kWh ($ 0.19 – 0.25/kWh), although current demonstration projects operate between EUR 0.25-0.47/kWh ($ 0.27–0.52/kWh). For wave energy, the projected a LCOE is the range of EUR 0.33-0.63/kWh ($0.37–0.70/kWh) for projects between 0.01 and 2 GW installed capacity, and EUR 0.113-0.226/kWh ($0.13 – 0.25/kWh) if deployment exceeds the 2 GW capacity. However, installing such a large WEC is yet not feasible due to the prohibitive initial investment, and is not projected to be viable at least until 2030 (IRENA, 2018).

Additionally, the U.S. DOE predicted a LCOE for the first commercial project in the range of $0.130–0.28/kWh for tidal energy, and $0.12–0.47/kWh. Moreover, significant cost reductions in the long term are expected as experience is gained in the field (USDOE, 2019).

Although predictions are promising for wave energy, there is not much information about the capital and operation cost of deployed wave energy systems. Research by The Faculty of California Polytechnic State University in 2010 evaluated the cost of electricity production of a few wave power systems at the time. An average rate of $0.28/kWh for the Pelamis and

$0.26/kWh for the 1.5 MW Wave Dragon were estimated (Jarocki, 2010). However, both systems were not successful, and there is not any other available data to confirm if these rates were achieved, thus the cost of electricity produced by wave energy converters remains uncertain.

There are numerous reasons why wave energy technologies are still far from being cost-competitive, including the elevated initial investment of designing, building, and operating a new power plant, compared to the continuous operation of already existing plants. However, this study suggests that the economic barrier can be easier to overcome if wave energy technologies focus first on specific locations where the cost of electricity is already high, or above average, before they can try to compete with cheaper and already established technologies. Experience has demonstrated that wave energy systems deployed in areas where electricity production is already cheap and comes from a wide variety of sources, such as the Limpet in Scotland, the Pelamis in Portugal, and Wave Dragon in Denmark, have not been successful and end up being dismantled after millions of dollars invested. A common factor found in these wave farms is that they were all implemented in regions were the dependency in fossil fuels is already moderate and continuously decreasing every year, being replaced from a wide variety of resources, mainly nuclear, hydro, wind, and solar (World Energy Council, 2019).

With current wave energy electricity rates estimated in the range of $0.32-0.60/kWh, all efforts should aim towards areas where the cost of electricity is already elevated, thus the difference between wave power and current technologies is minimized. Less populated or remote areas usually result in a higher average electric rate, making wave energy a more suitable alternative than current resources. For instance, Hawaii has currently the most elevated cost of

electricity generation in the U.S. with an average of $0.29/kWh (EIA, 2019). This means that current wave technologies can compete with these rates and become a viable alternative.

According to the DOE Annual Energy Consumption and the EIA, the 2018 United States average electricity rate was 10.50¢/kWh. The location selected for this work is Fernandina Beach, Florida, which has an average rate of 13.02¢/kWh. Although the energy rate here is not significantly higher than the United States average, it is still 26% greater than the Florida average rate of 10.31¢/kWh (EIA, 2019).

9. Conclusion

Many different types of wave energy converters have been tested and implemented up to date, however, only a few have been successful, and are currently supplying electricity to the power grid. Wave energy has the potential to contribute to the global energy demand, by overcoming both the environmental impact from fossil fuel resources, and the availability and predictability of other renewable energies such as wind and solar.

This work is the first stage of the design process of a wave energy converter. This study suggests that the idea of using the electromagnetic induction principle to generate electricity from the upward and downward movement of ocean waves can be achieved. Although the system's design has not been yet finalized, two different models were numerically analyzed. The initial idea consists of a floating body connected to a permanent magnet that will move along a coil of wire enclosed in a fixed structure. Two different body shapes, a sphere and a cylinder, were modeled and analyzed numerically to analyze their behavior and to compare the different forces acting on each model. It can be concluded from this work that there was not a significant

difference between one or the other, being the sphere body the one that suffered slightly lower hydrodynamic forces. It was also verified that the hydrodynamic forces computed numerically match similarly with the forces computed in MATLAB using the ocean data obtained from the NOAA. Additionally, the economic analysis suggests that, with the elevated cost of current wave energy technologies, there will still be at least a few years until these technologies are more developed and therefore more costly-efficient. However, certain regions that have difficulty accessing to energy sources, such as Hawaii in the United States, and many other islands and remote locations where the electricity cost is already elevated, wave energy can be a feasible solution if all efforts focus on that.

To conclude, this initial investigation can lead to the design of a WEC system with the potential to overcome previous challenges from unsuccessful devices, and to overcome the economic barrier that is slowing the development of these technologies.

10. Future Work

This work was just the beginning of the design process of a WEC system. To continue this research, the following future steps are suggested: (1) To evaluate the proposed ideas, and conclude with a final design; (2) To perform dimensional analysis from the wave data analyzed in this work to set up the wave tank conditions; (3) To experimentally test a small-scale model of the finalized prototype; (4) To verify experimental results with numerical modeling results, and vice versa; (5) To investigate different types of mooring configurations for the system; (6); To evaluate the environmental impacts of the finalized prototype (7) To estimate the LCOE of the proposed system.

APPENDIX A: Hydrodynamic Diffraction

Appendix A.1.a. Cylinder Hydrostatic Results

Hydrostatic Stiffness						
Center of Gravity (CoG) Position:	X:	-1.1923e-7 m	Y:	1.8957e-9 m	Z:	0.5 m
		Z		RX		RY
Heave (Z):		17743.957 N/m		4.3911e-7 N/°		6.183e-4 N/°
Roll (RX):		2.5159e-5 N.m/m		-72.635429 N.m/°		8.7132e-6 N.m/°
Pitch (RY):		3.5426e-2 N.m/m		8.7132e-6 N.m/°		-72.635956 N.m/°
Hydrostatic Displacement Properties						
Actual Volumetric Displacement:		0.882663 m³				
Equivalent Volumetric Displacement:		1.9512e-2 m³				
Center of Buoyancy (CoB) Position:	X:	-1.1923e-7 m	Y:	3.0497e-9 m	Z:	-0.2500011 m
Out of Balance Forces/Weight:	FX:	-3.7927e-7	FY:	3.6845e-6	FZ:	44.236469
Out of Balance Moments/Weight:	MX:	-1.494e-6 m	MY:	-1.2205e-6 m	MZ:	-6.0495e-9 m
Cut Water Plane Properties						
Cut Water Plane Area:		1.7652488 m²				
Center of Floatation:	X:	-2.1158e-6 m	Y:	3.3136e-9 m		
Principal 2nd Moments of Area:	X:	0.2479702 m⁴	Y:	0.2479732 m⁴		
Angle between Principal X Axis and Global X Axis:		89.064217°				
Small Angle Stability Parameters	*with respect to Principal Axes*					
CoG to CoB (BG):		0.7500011 m				
Metacentric Heights (GMX/GMY):		-0.469067 m		-0.4690635 m		
CoB to Metacentre (BMX/BMY):		0.2809342 m		0.2809376 m		
Restoring Moments (MX/MY):		-72.635956 N.m/°		-72.635422 N.m/°		

Appendix A.1.b. Sphere Hydrostatic Results

Hydrostatic Stiffness						
Center of Gravity (CoG) Position:	X:	4.446e-6 m	Y:	2.1951e-6 m	Z:	0. m
		Z		RX		RY
Heave (Z):		17744.787 N/m		-7.2132e-4 N/°		1.3951e-3 N/°
Roll (RX):		-4.1328e-2 N.m/m		9.8454e-2 N.m/°		-2.13e-6 N.m/°
Pitch (RY):		7.9936e-2 N.m/m		-2.13e-6 N.m/°		9.8465e-2 N.m/°
Hydrostatic Displacement Properties						
Actual Volumetric Displacement:		0.8807524 m³				
Equivalent Volumetric Displacement:		1.9512e-2 m³				
Center of Buoyancy (CoB) Position:	X:	4.4512e-6 m	Y:	2.1634e-6 m	Z:	-0.2809338 m
Out of Balance Forces/Weight:	FX:	-4.0285e-6	FY:	-1.0264e-6	FZ:	44.138573
Out of Balance Moments/Weight:	MX:	-6.039e-7 m	MY:	-4.767e-7 m	MZ:	2.2527e-8 m
Cut Water Plane Properties						
Cut Water Plane Area:		1.7653314 m²				
Center of Floatation:	X:	-5.8757e-8 m	Y:	-1.3394e-7 m		
Principal 2nd Moments of Area:	X:	0.2479943 m⁴	Y:	0.2479943 m⁴		
Angle between Principal X Axis and Global X Axis:		0.°				
Small Angle Stability Parameters		*with respect to Principal Axes*				
CoG to CoB (BG):		0.2809338 m				
Metacentric Heights (GMX/GMY):		6.3717e-4 m		6.3723e-4 m		
CoB to Metacentre (BMX/BMY):		0.2815709 m		0.281571 m		
Restoring Moments (MX/MY):		9.8454e-2 N.m/°		9.8463e-2 N.m/°		

Appendix A.2.a.ii. Cylinder Froude-Krylov - Force/Moment vs Frequency (N/m) – Global X @ h = 3 m.

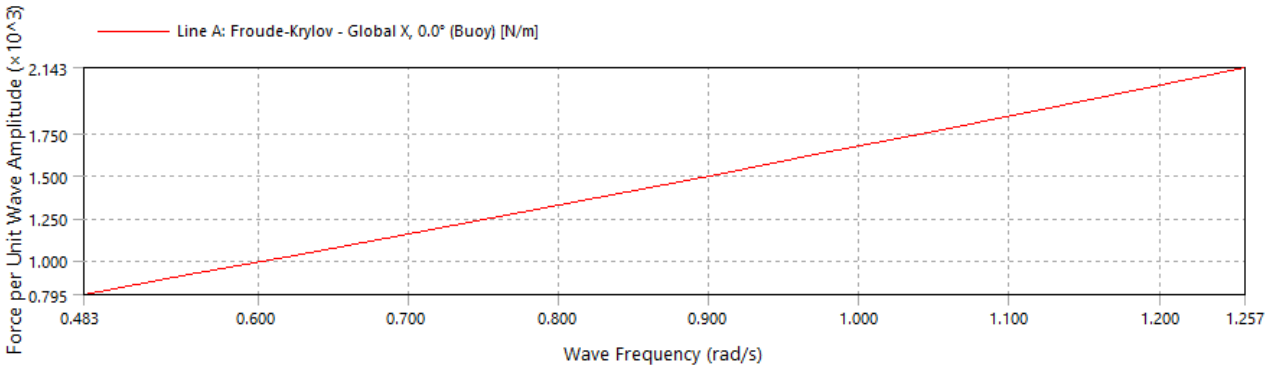

Appendix A.2.a.ii Cylinder Froude-Krylov - Force/Moment vs Frequency (N/m) – Global X @ h = 15 m.

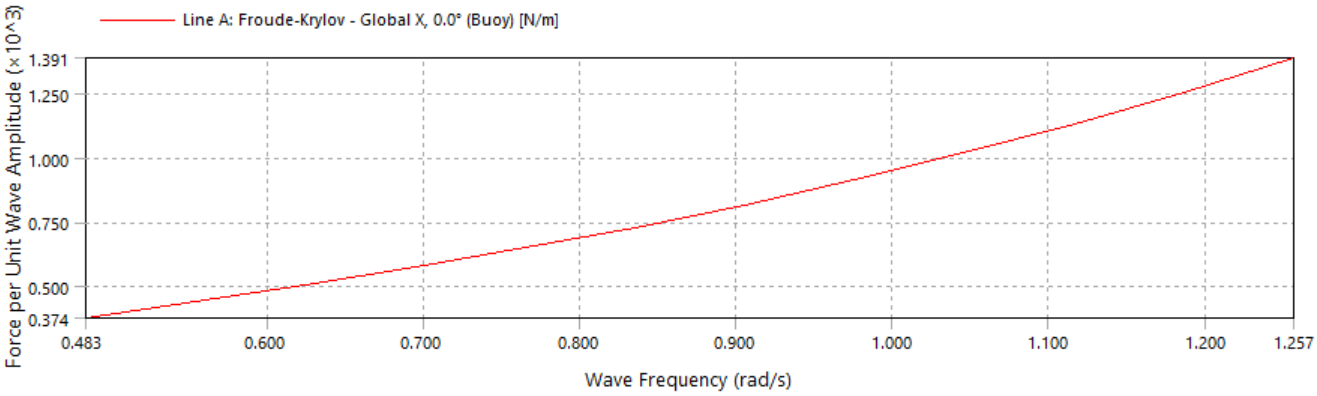

Appendix A.2.b.i Sphere Froude-Krylov - Force/Moment vs Frequency (N/m) – Global X @ h = 3 m.

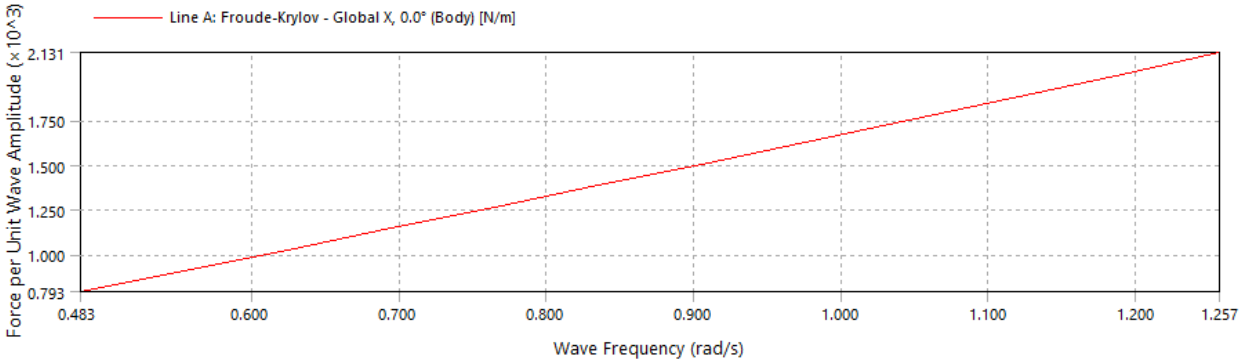

Appendix A.2.b.ii Sphere Froude-Krylov - Force/Moment vs Frequency (N/m) – Global X @ h = 15 m.

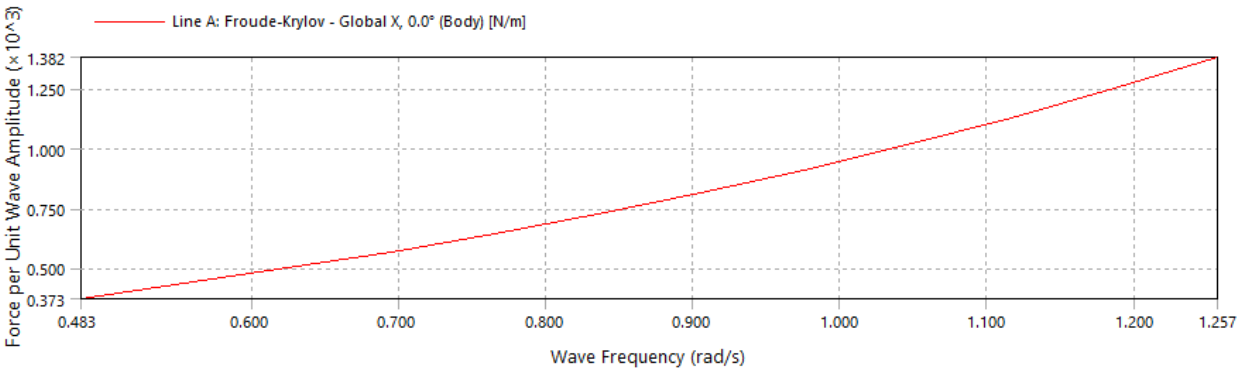

Appendix A.3.a.i Cylinder Froude-Krylov - Force/Moment vs Frequency (N/m) – Global Z @ h = 3 m

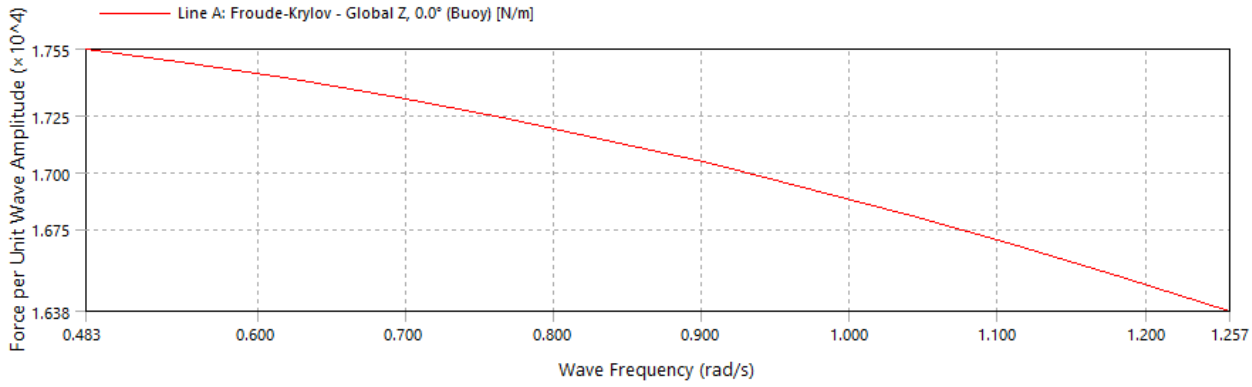

Appendix A.3.a.ii Cylinder Froude-Krylov - Force/Moment vs Frequency (N/m) – Global Z @ h = 15 m

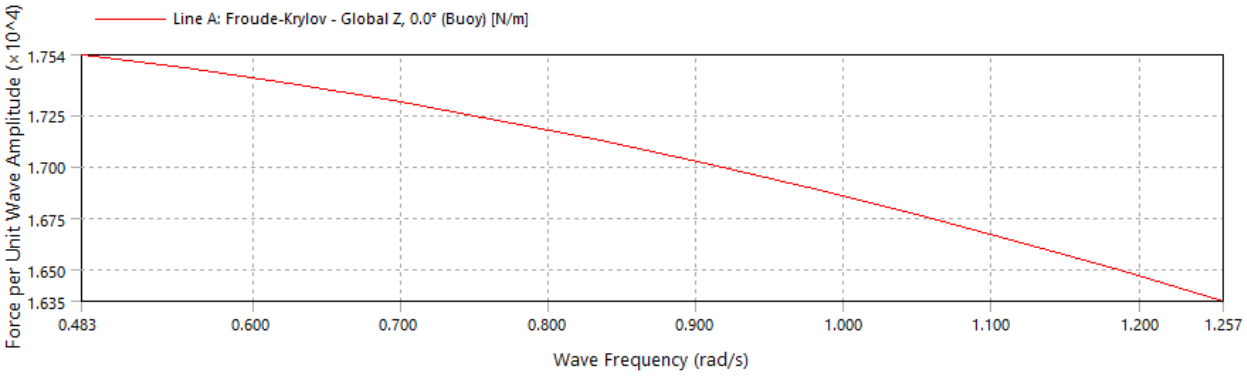

Appendix A.3.b.i Sphere Froude-Krylov - Force/Moment vs Frequency (N/m) – Global Z @ h = 3 m.

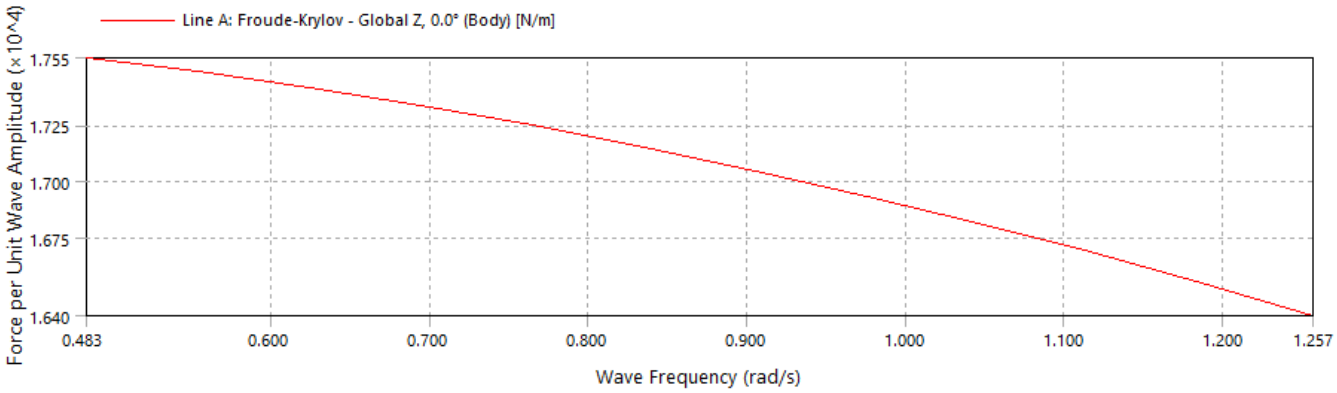

Appendix A.3.b.i Sphere Froude-Krylov - Force/Moment vs Frequency (N/m) – Global Z @ h = 15 m.

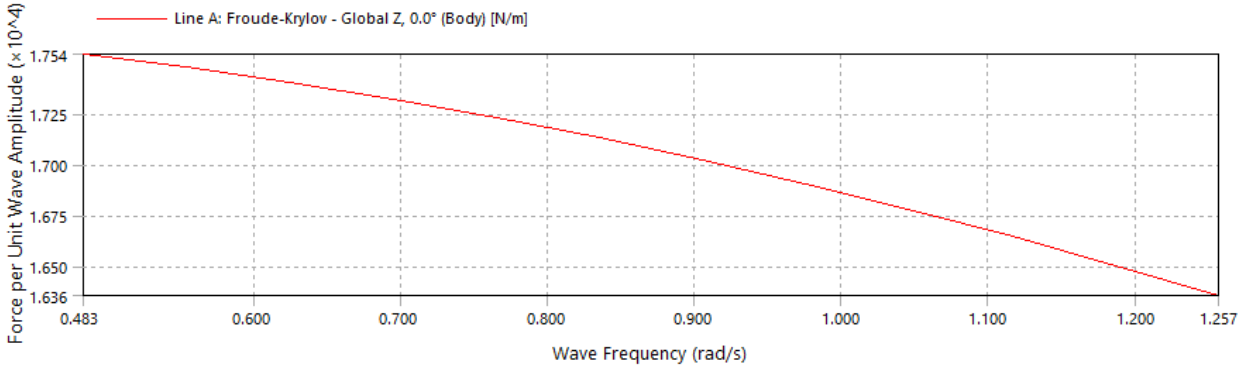

Appendix A.4.a.i Cylinder Diffraction - Force/Moment vs Frequency (N/m) @ h = 3 m.

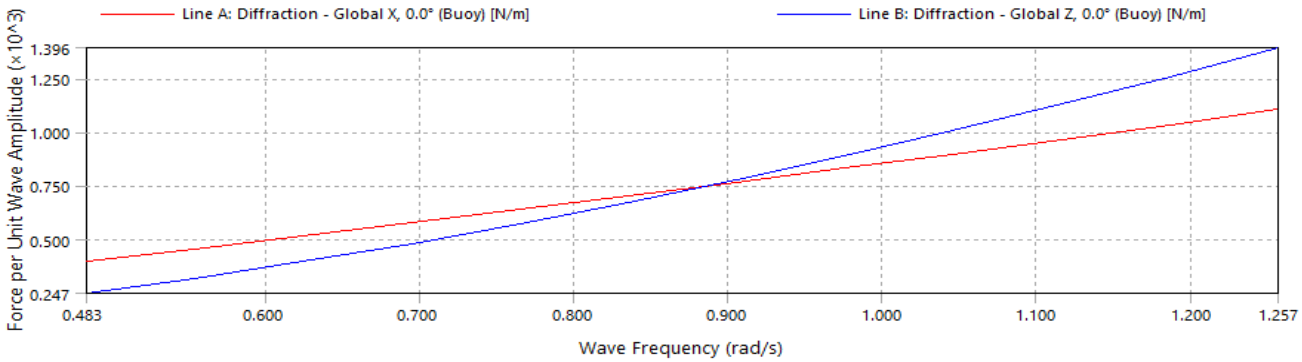

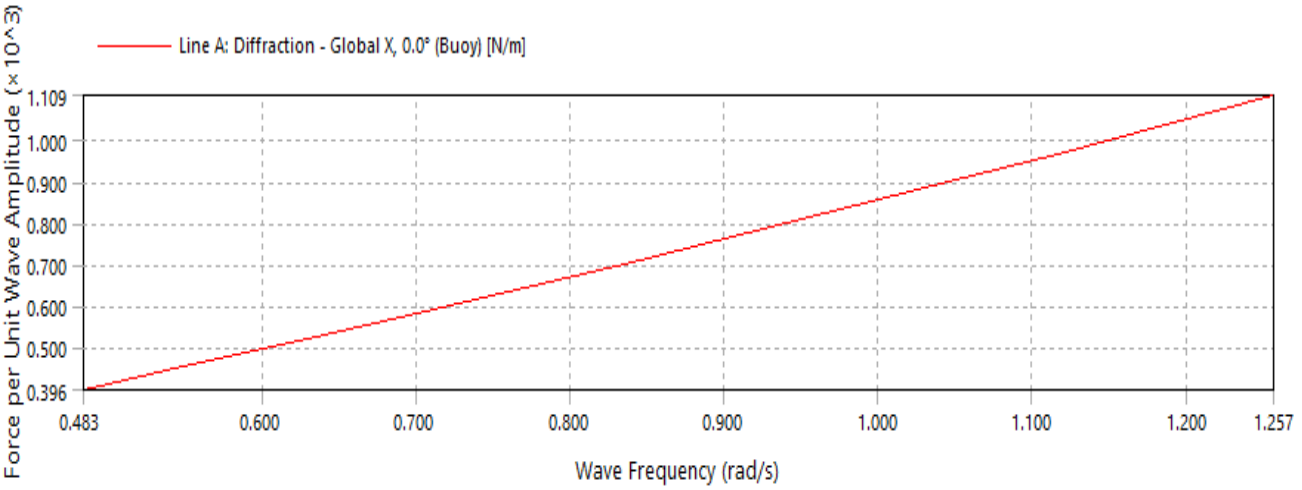

Appendix A.4.a.ii Cylinder Diffraction - Force/Moment vs Frequency (N/m) @ h = 15 m.

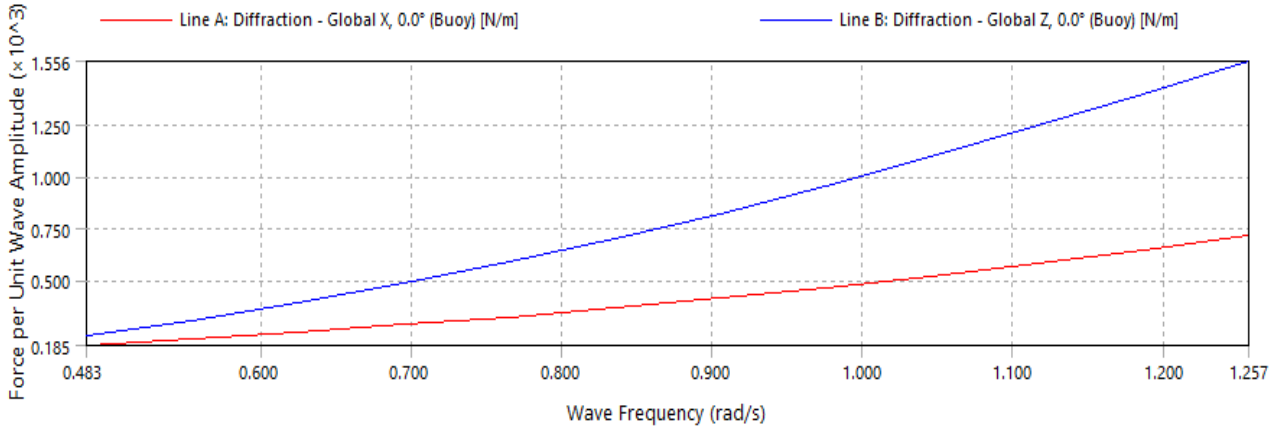

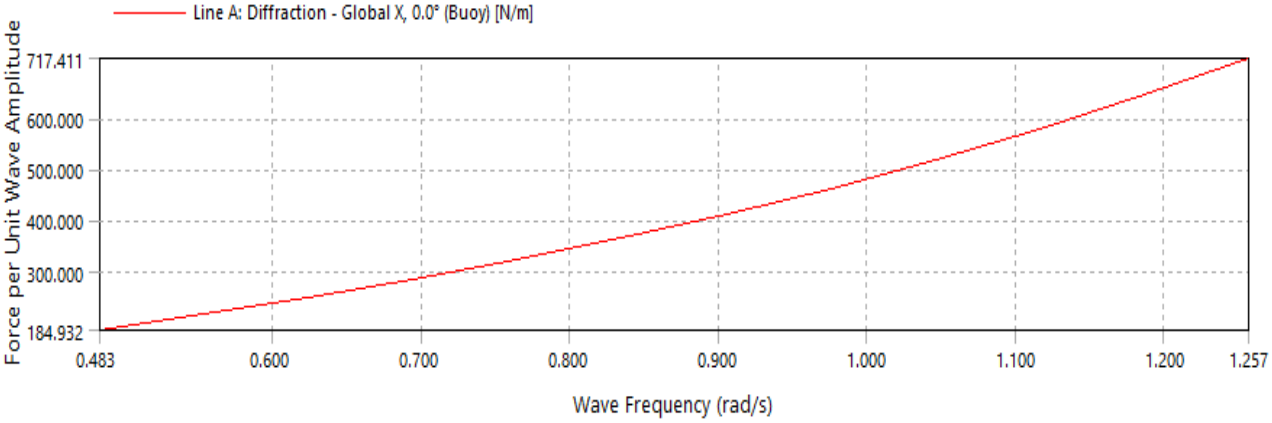

Appendix A.4.b.a Sphere Diffraction - Force/Moment vs Frequency (N/m) @ h = 3 m.

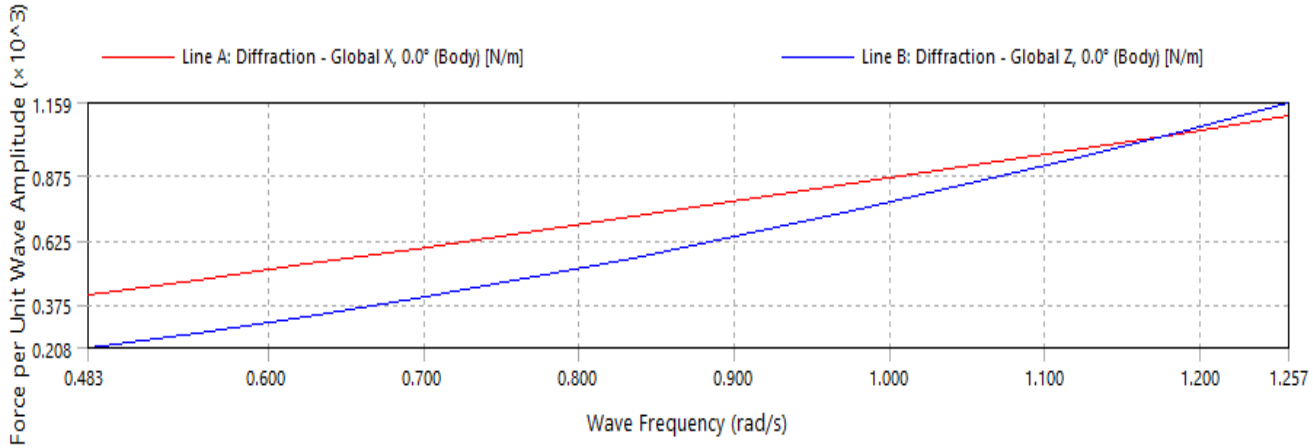

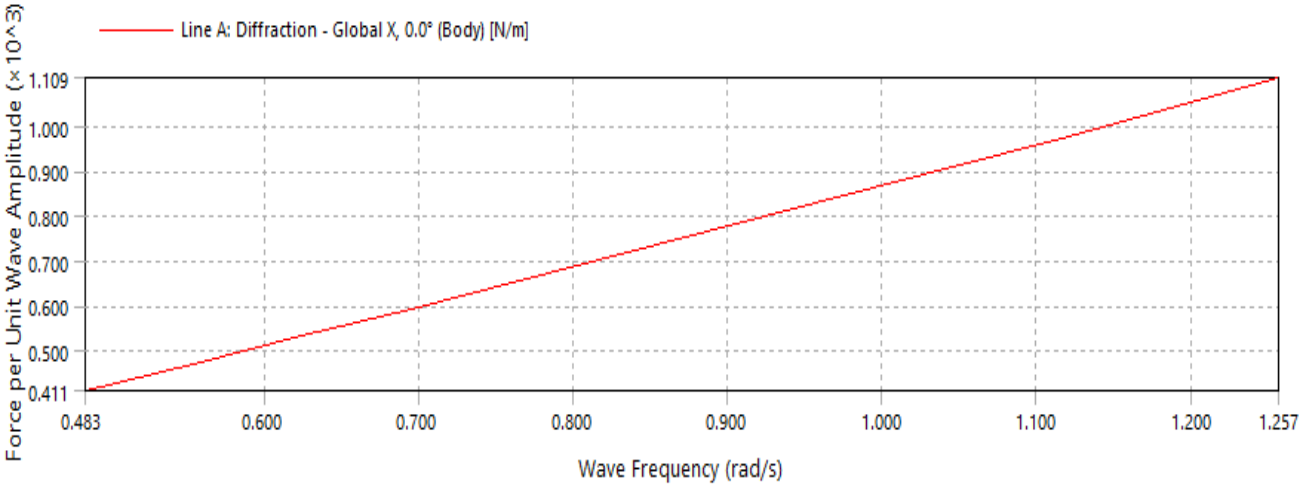

Appendix A.4.b.b Sphere Diffraction - Force/Moment vs Frequency (N/m) @ h = 15 m.

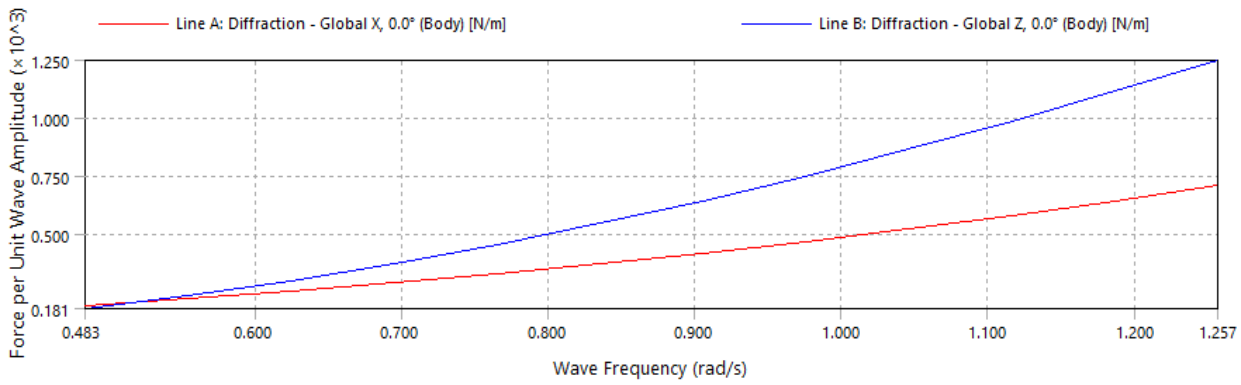

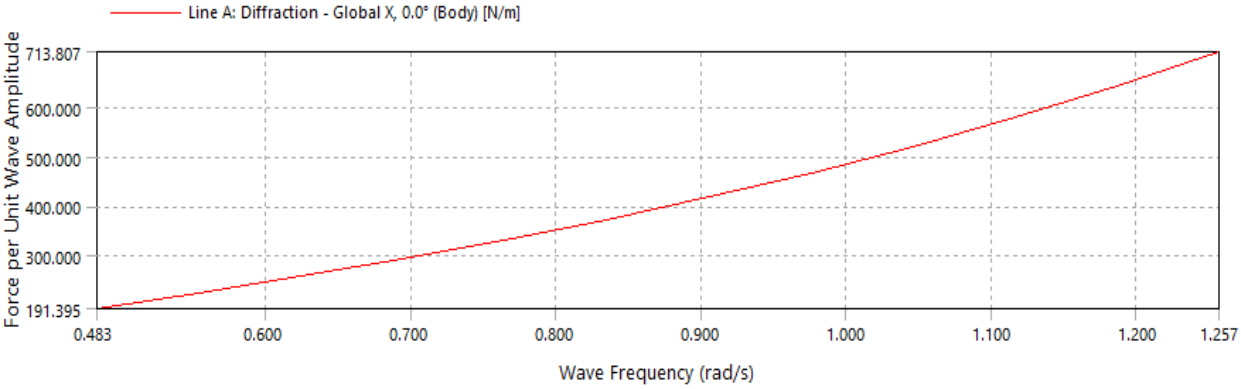

Appendix A.5.a.i Cylinder Radiation Damping - Force/Moment vs Frequency (N/m) @ h = 3 m.

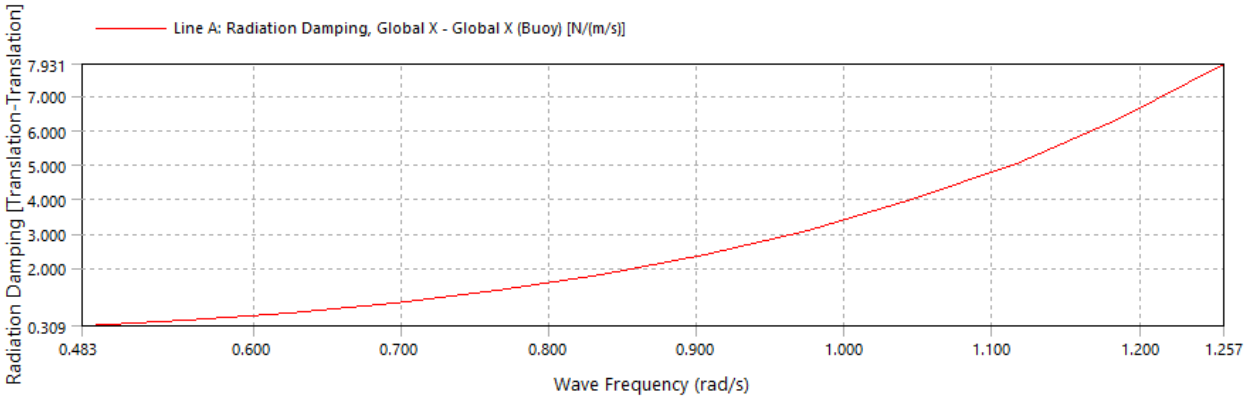

Appendix A.5.a.ii Cylinder Radiation Damping - Force/Moment vs Frequency (N/m) @ h = 15 m.

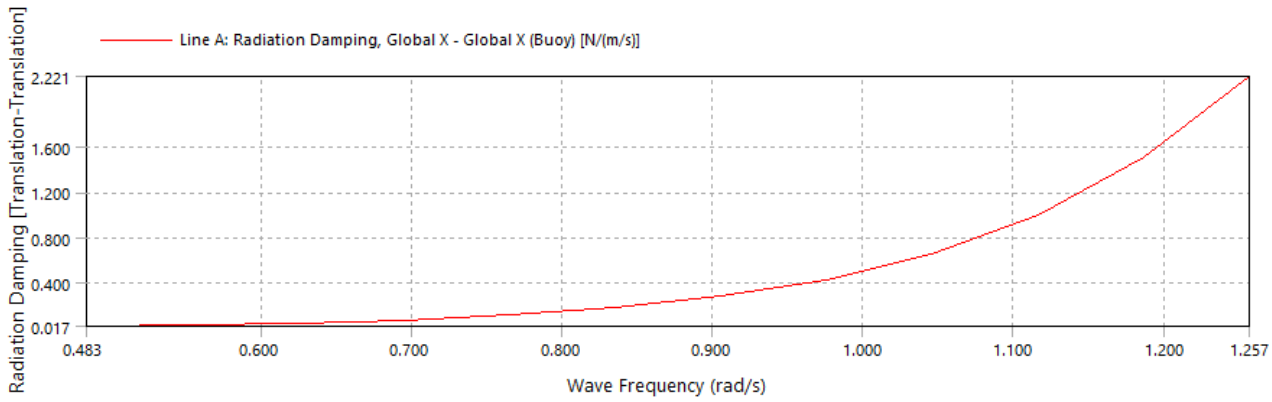

Appendix A.5.b.i Sphere Radiation Damping - Force/Moment vs Frequency (N/m) @ h = 3 m.

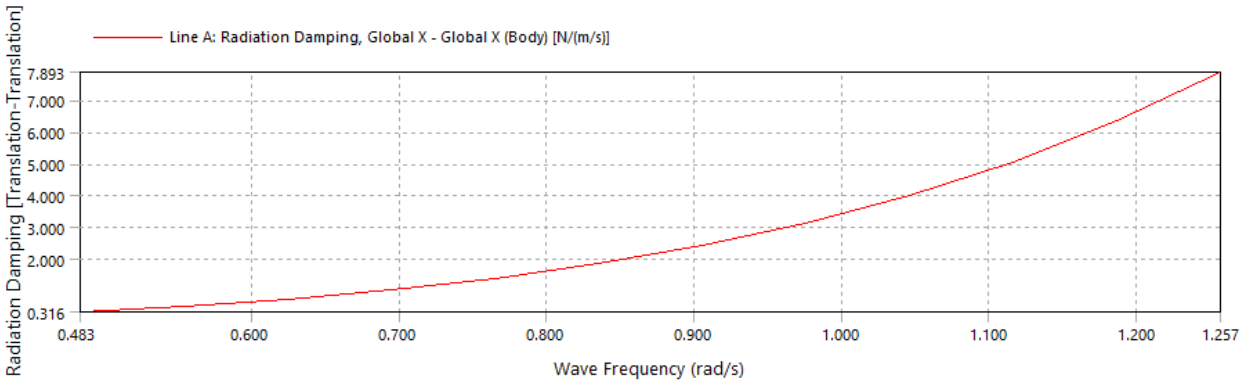

Appendix A.5.b.ii Sphere Radiation Damping - Force/Moment vs Frequency (N/m) @ h = 15 m.

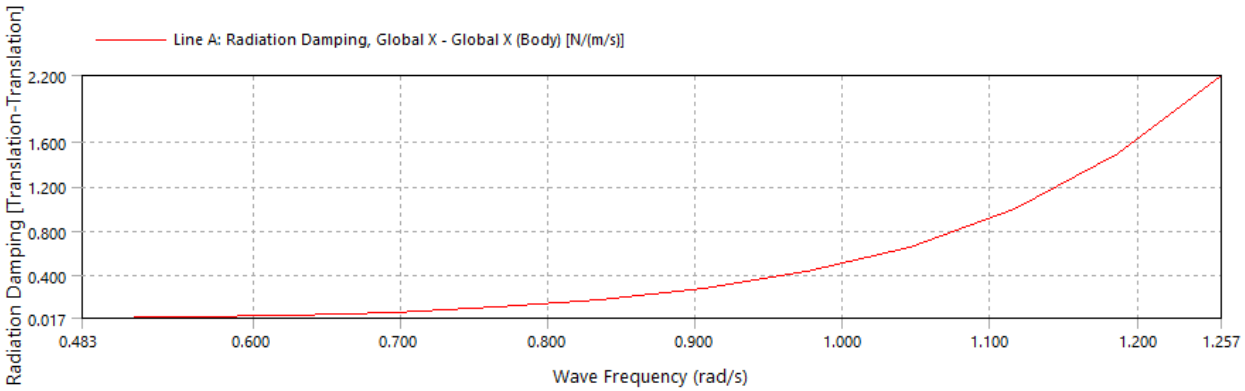

Appendix B. Static Stability Analysis

Appendix B1. Natural Modes

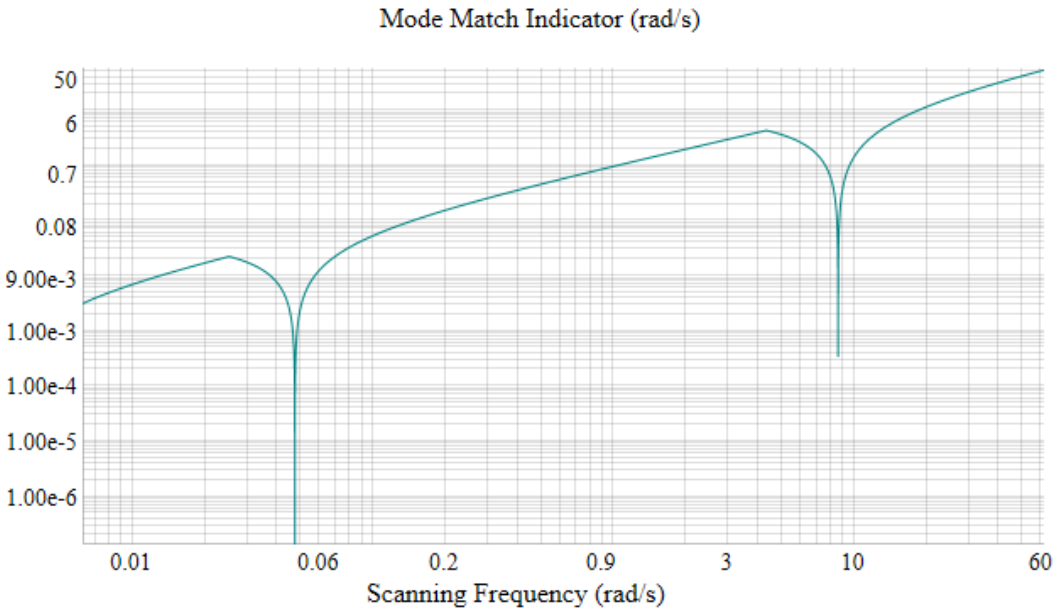

Appendix C. Time Response Analysis

Appendix C.1.a. Cylinder Structure Position, RAO Based Response @ h = 3 meters

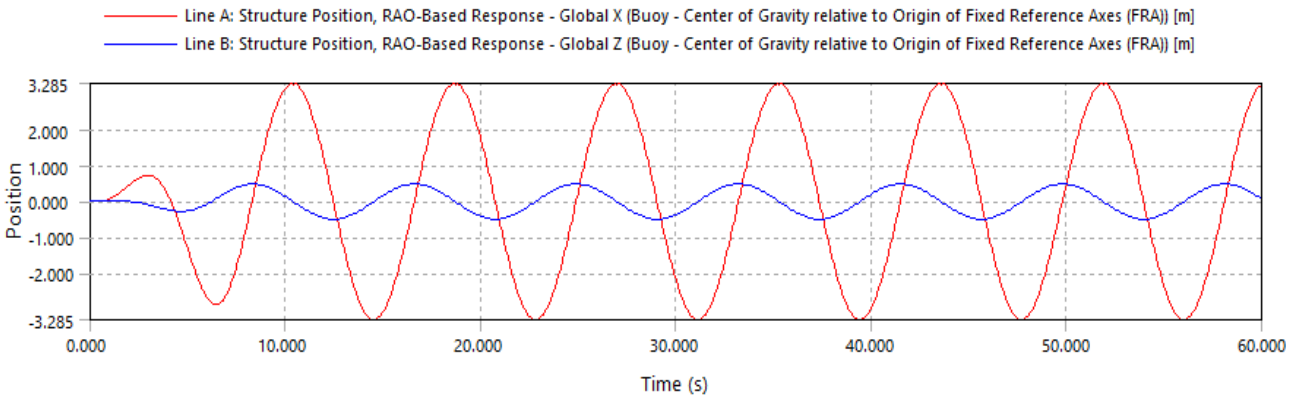

Appendix C.2.a. Cylinder Structure Position, RAO Based Response @ h = 15 meters

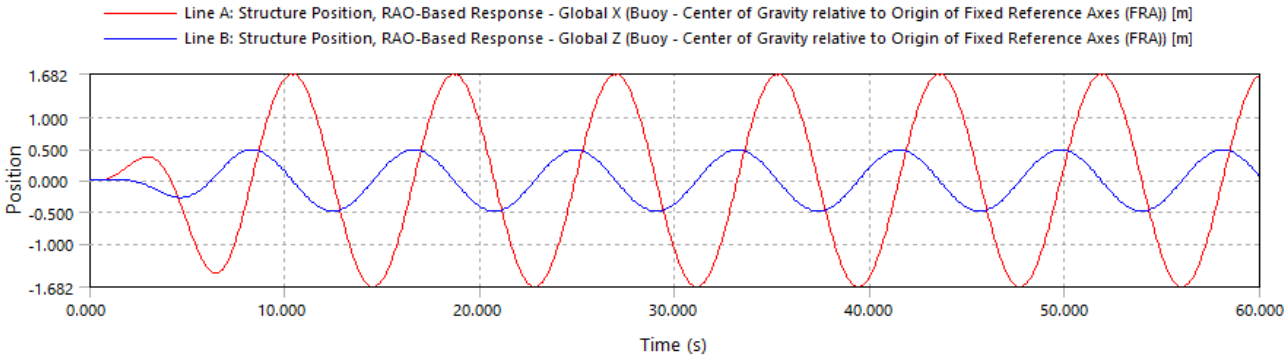

Appendix C.1.b. Sphere Structure Position, RAO Based Response @ h = 3 meters

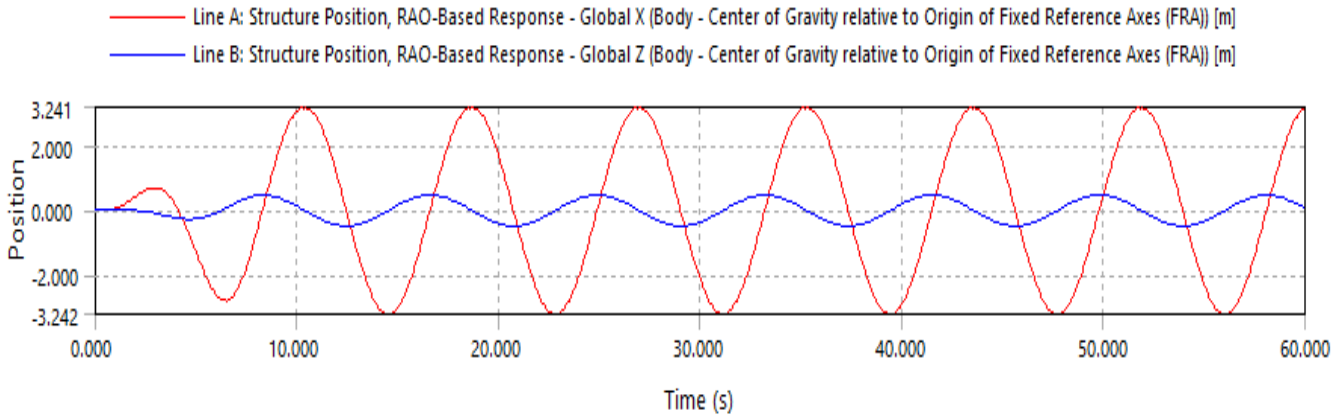

Appendix C.2.b. Sphere Structure Position, RAO Based Response @ h = 15 meters

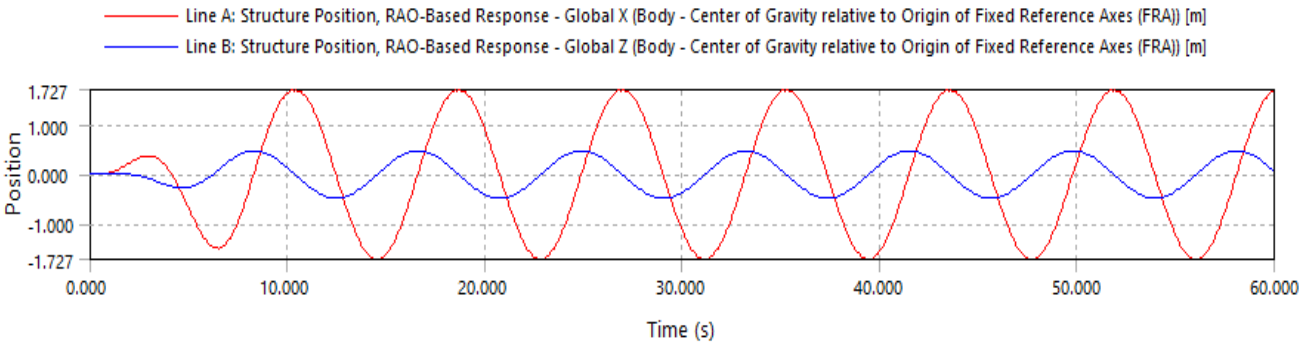

Appendix D. Frequency Response Analysis

Appendix D.1.a.i Cylinder Wave Spectra Response @ h = 3 m.

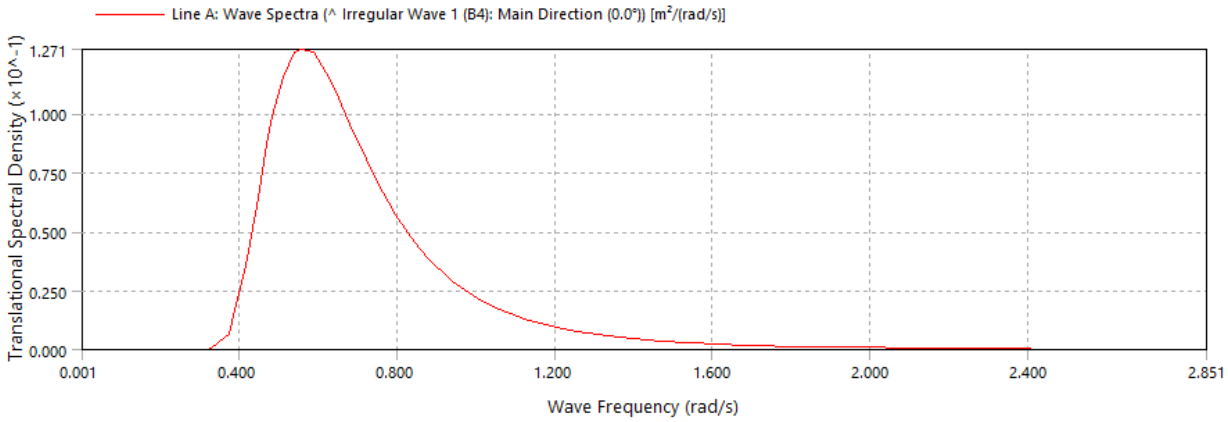

Appendix D.1.a.ii Cylinder Wave Spectra Response @ h = 15 m.

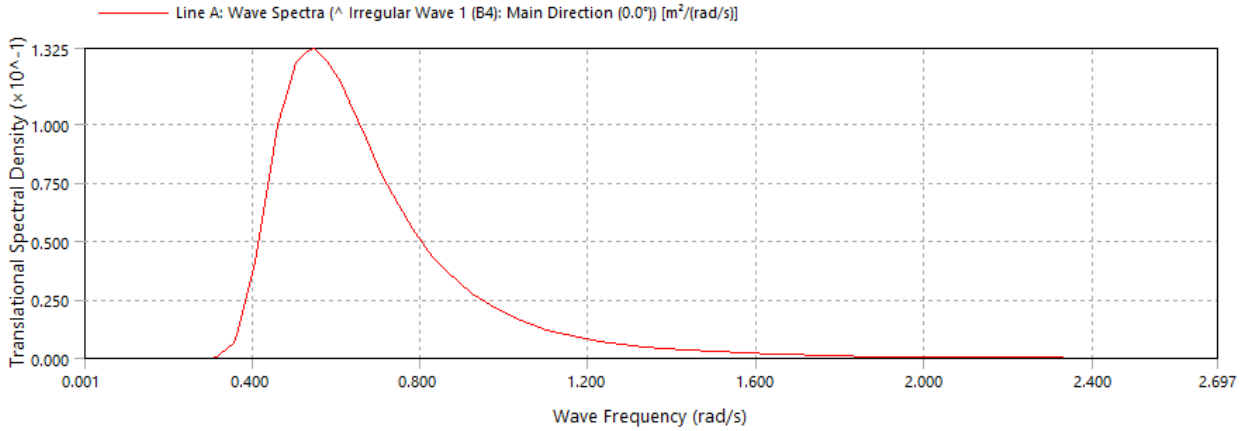

Appendix D.1.b. Sphere Wave Spectra Response @ h = 3 m

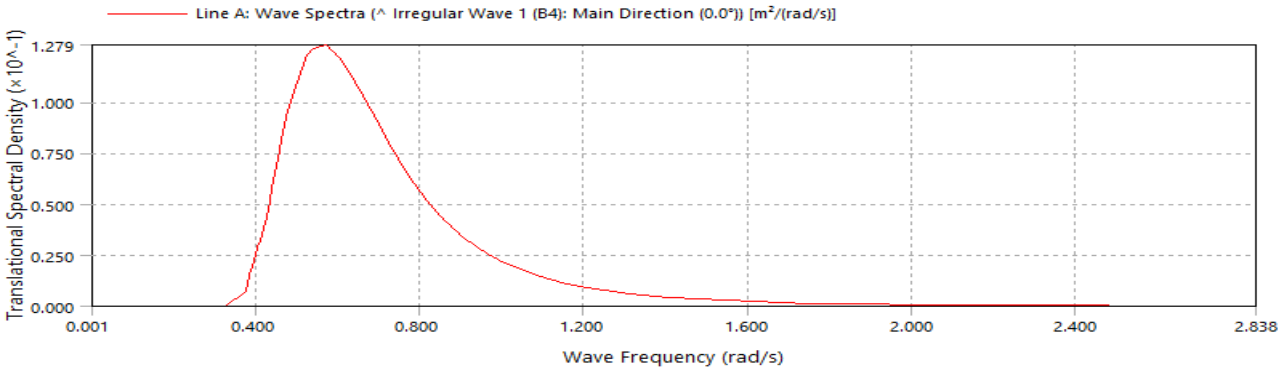

Appendix D.1.b.ii Sphere Wave Spectra Response @ h = 15 m

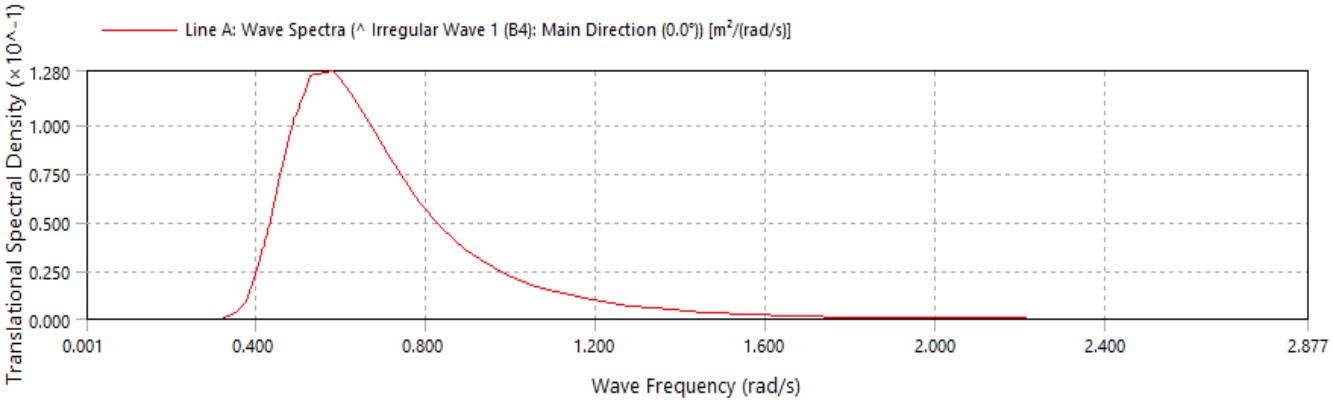

Appendix D.2.a. Frequency Domain Statistics Results of Cylinder @ h = 3 m.

Cylinder						
Significant Value (Amplitude)						
Motions:	*at Center of Gravity, in Local Structure Axes*					
Position	X:	3.8051 E-8 m	Y:	3.9069 E-8 m	Z:	3.8012 E-7 m
Velocity	X:	3.6015 E-8 m/s	Y:	3.6977 E-8 m/s	Z:	2.7217 E-7 m/s
Acceleration	X:	4.7081 E-8 m/s²	Y:	4.8339 E-8 m/s²	Z:	2.7302 E-7 m/s²
Expected Extreme, Duration: 3 hours						
Motions:	*at Center of Gravity, in Local Structure Axes*					
Position	X:	7.4779 E-8 m	Y:	7.6777 E-8 m	Z:	7.4701 E-7 m
Velocity	X:	7.0776 E-8 m/s	Y:	7.2668 E-8 m/s	Z:	5.3486 E-7 m/s
Acceleration	X:	9.2523 E-8 m/s²	Y:	9.4997 E-8 m/s²	Z:	5.3654 E-7 m/s²
Probable Maximum, Duration: 3 hours						
Motions:	*at Center of Gravity, in Local Structure Axes*					
Position	X:	7.1931 E-8 m	Y:	7.3854 E-8 m	Z:	7.1857 E-7 m
Velocity	X:	6.8081 E-8 m/s	Y:	6.9901 E-8 m/s	Z:	5.1450 E-7 m/s
Acceleration	X:	8.9000 E-8 m/s²	Y:	9.1380 E-8 m/s²	Z:	5.1611 E-7 m/s²

Appendix D.2.a.ii Frequency Domain Statistics Results of Cylinder @ h = 15 m.

Cylinder						
Significant Value (Amplitude)						
Motions:	*at Center of Gravity, in Local Structure Axes*					
Position	X:	0.00415 m	Y:	6.0878 E-6 m	Z:	3.7770 E-7 m
Velocity	X:	0.00428 m/s	Y:	5.3947 E-7 m/s	Z:	2.7036 E-7 m/s
Acceleration	X:	0.00598 m/s²	Y:	5.7276 E-7 m/s²	Z:	2.6977 E-7 m/s²
Expected Extreme, Duration: 3 hours						
Motions:	*at Center of Gravity, in Local Structure Axes*					
Position	X:	0.00816 m	Y:	1.1964 E-5 m	Z:	7.4226 E-7 m
Velocity	X:	0.00841 m/s	Y:	1.0602 E-6 m/s	Z:	5.3131 E-7 m/s
Acceleration	X:	0.01174 m/s²	Y:	1.1256 E-6 m/s²	Z:	5.3015 E-7 m/s²
Probable Maximum, Duration: 3 hours						
Motions:	*at Center of Gravity, in Local Structure Axes*					
Position	X:	0.00785 m	Y:	1.1508 E-5 m	Z:	7.1400 E-7 m
Velocity	X:	0.00809 m/s	Y:	1.0198 E-6 m/s	Z:	5.1108 E-7 m/s
Acceleration	X:	0.01130 m/s²	Y:	1.0827 E-6 m/s²	Z:	5.0996 E-7 m/s²

Appendix D.2.b. Frequency Domain Statistics Results of Sphere @ h = 3m.

Sphere						
Significant Value (Amplitude)						
Motions:	*at Center of Gravity, in Local Structure Axes*					
Position	X:	0.06532 m	Y:	73650.56250 m	Z:	0.44142 m
Velocity	X:	0.06338 m/s	Y:	26.35201 m/s	Z:	0.33820 m/s
Acceleration	X:	0.08536 m/s²	Y:	0.06083 m/s²	Z:	0.38428 m/s²
Expected Extreme, Duration: 3 hours						
Motions:	*at Center of Gravity, in Local Structure Axes*					
Position	X:	0.12868 m	Y:	1.4508 E+5 m	Z:	0.86955 m
Velocity	X:	0.12484 m/s	Y:	51.91023 m/s	Z:	0.66621 m/s
Acceleration	X:	0.16815 m/s²	Y:	0.11984 m/s²	Z:	0.75699 m/s²
Probable Maximum, Duration: 3 hours						
Motions:	*at Center of Gravity, in Local Structure Axes*					
Position	X:	0.12380 m	Y:	1.3959 E+5 m	Z:	0.83660 m
Velocity	X:	0.12011 m/s	Y:	49.94326 m/s	Z:	0.64096 m/s
Acceleration	X:	0.16178 m/s²	Y:	0.11530 m/s²	Z:	0.72830 m/s²

Appendix D.2.b.ii Frequency Domain Statistics Results of Sphere @ h = 15 m.

Sphere						
Significant Value (Amplitude)						
Motions:	*at Center of Gravity, in Local Structure Axes*					
Position	X:	0.00035 m	Y:	0.00042 m	Z:	3.7911 E-8 m
Velocity	X:	0.00037 m/s	Y:	0.00046 m/s	Z:	2.8270 E-8 m/s
Acceleration	X:	0.00052 m/s²	Y:	0.00066 m/s²	Z:	2.9672 E-8 m/s²
Expected Extreme, Duration: 3 hours						
Motions:	*at Center of Gravity, in Local Structure Axes*					
Position	X:	0.00069 m	Y:	0.00083 m	Z:	7.4679 E-8 m
Velocity	X:	0.00072 m/s	Y:	0.00090 m/s	Z:	5.5688 E-8 m/s
Acceleration	X:	0.00102 m/s²	Y:	0.00131 m/s²	Z:	5.8450 E-8 m/s²
Probable Maximum, Duration: 3 hours						
Motions:	*at Center of Gravity, in Local Structure Axes*					
Position	X:	0.00067 m	Y:	0.00080 m	Z:	7.1850 E-8 m
Velocity	X:	0.00069 m/s	Y:	0.00086 m/s	Z:	5.3578 E-8 m/s
Acceleration	X:	0.00098 m/s²	Y:	0.00126 m/s²	Z:	5.6235 E-8 m/s²

References

Aderinto, T. & Li, H. (May 2018). Ocean Wave Energy Converters: Status and Challenges.

Aderinto, T. & Li, H. (2019). Review on Power Performance and Efficiency of Wave Energy Converters.

Anderson, C. (2003). Pelamis WEC-Main Body Structural Design and Materials Selection. *Ocean Power Delivery Ltd.: Edinburgh, UK.*

Angelis-Dimakis, A. et al. (2010). Methods and tools to evaluate the availability of renewable energy sources

ANSYS, Inc. (October 2012). AQWA User Manual

Astariz S, Iglesias G. (2015). Enhancing wave energy competitiveness through co-located wind and wave energy farms. A review on the shadow effect.

Bald, J. (October 2019). Mutriku Wave Energy Plant, Bay of Biscay, Basque Country. Retrieved from https://www.renewable-technology.com/projects/mutriku-wave-energy-plant/

Bankestad, M. (2013). Modeling, Simulation and Dynamic Control of a Wave Energy Converter.

Beatty, J. S. (2003). Analysis and Development of a Three Body Heaving Wave Energy Converter.

Boake C. B., Whittaker, T., Folley, M. & Ellen, H. (May 2002). Overview and Initial Operational Experience of the LIMPET Wave Energy Plant.

Borthwick, A. (2016). Marine Renewable Energy Seascape. *Renewable Energy Review, pages 69-78.*

Boserelle, C., Reddy, S. K. & Kruger, J. (November 2015). Cost Analysis of Wave Energy in the Pacific. *Waves and Coasts in the Pacific.*

Bostrom, C. (2011). Electrical Systems for Wave Energy Conversion. *Uppsala Universitet. Retrieved from* *http://www.diva-portal.org/smash/get/diva2:383042/FULLTEXT02*

Cai, R., Yang, H., He, J. et al. (2009). The effects of magnetic fields on water molecular hydrogen bonds. pp. 15-19

Dean, R. & Dalrymple, R. (1991). Water Wave Mechanics for Engineers and Scientists. *World Scientific*

Drew, B., Plummer, A. R., & Sahinkaya, M. N. (2009). A Review of Wave Energy Converter Technology. *Department of Mechanical Engineering, University of Bath, Bath, UK.*

Jarocki, D. (March 2010). Wave Energy Converter Performance Modeling and Cost of Electricity Assessment.

Edwards, K. & Mekhiche, M. (April 2013). Ocean Testing of a Wave-Capturing Power Buoy. *Ocean Power Technologies (OPT). Retrieved from* *https://www.oceanpowertechnologies.com/uploads/10fac4f75ab4d841abb198d8eb96488e.pdf*

Energy Information Administration (EIA). (July 2016). Fossil Fuels Still Dominate U.S. Energy Consumption Despite Recent Market Share Decline.

Engström, J., Kurupath, V., Isberg, J. & Leijon, M. (2011). A resonant two body system for a point absorbing wave energy converter with direct-driven linear generator. *Journal of Applied Physics. 110.*

European Marine Energy Centre (EMEC). (2009). Guidelines for Reliability, Maintainability and Survivability of Marine Energy Conversion Systems.

European Marine Energy Centre (EMEC). (July 2017). Press Release: Council Takes Ownership of Pelamis Device.

Faizal, M., Ahmed, M. R. & Lee, Y. (2014). A Design Outline for a Floating Point Absorber Wave Energy Converters.

Falcao, A. (2014). Modelling of Wave Energy Conversion. *Instituto Superior Tecnico, Universidad Tecnica de Lisboa.*

Falnes, J. (June 2007). A Review of Wave Energy Extraction.

Fetisov, L. Y., Serov, V. N., Chashin, D. V., Makovin, S. A., Srinivasan, G., Viehland, D. & Fetisov, Y. K. (2017). A magnetoelectric sensor of threshold DC magnetic fields. *Journal of Applied Physics 121.*

Fisher, C. & Slater, M. (September 2010). Effects of electromagnetic fields on marine species: A literature review. *Oregon Wave Energy Trust*

Fontes, P. & Pereira, C. (May 2014). Design and Analysis of Buoy Geometries for a Wave Energy Converter.

Gomes Martins, E. E. (June 2014). Risk Assessment of Ocean Energy Projects. *Instituto Superior Tecnico de Lisboa.*

Hans Chr. Sørensen & Erik Friis-Madsen. (September, 2015). Wave Dragon 1.5 MW North Sea Demonstrator Phase 1.

Hewlett, R. (May 2016). Wave Star: Harnessing Ocean Waves from Unlimited Clean Energy. *Wave Star Energy.*

Holysz, L., Szczes, A. & Chibowski, E. (2007). Effects of a static magnetic field on water and electrolyte solutions.

Hovland, J. Paasch, R., & Haller, M. (June 2010). Characterizing Dangerous Waves for Ocean Wave Energy Converter Survivability.

IARC Working Group on the Evaluation of Carcinogenic Risk to Humans. (2002). Sources, Exposure and Exposure Assessment. *Retrieved from https://www.ncbi.nlm.nih.gov/books/NBK390728/*

International Ship and Offshore Structures Congress (ISSC) (January 2018). Offshore Renewable Energy. *Proceedings of the 20th ISSC 2018 Volume II – M.L. Kaminski and P. Rigo (Eds.). Retrieved from https://www.researchgate.net/publication/326261155_ISSC_2018_committee_V4_OFFSHORE_RENEWABLE_ENERGY.*

IRENA (2019). Renewable Power Generation Costs in 2018. *International Renewable Energy Agency, Abu Dhabi. Retrieved from https://www.irena.org/-*

/media/Files/IRENA/Agency/Publication/2019/May/IRENA_Renewable-Power-Generations-Costs-in-2018.pdf

IRENA (June 2014). Wave Energy. *Ocean Energy Technology Brief 4. Retrieved from* https://www.irena.org/documentdownloads/publications/wave-energy_v4_web.pdf

IRENA (June 2014). Tidal Energy. *Ocean Energy Technology Brief 4. Retrieved from* https://www.irena.org/documentdownloads/publications/tidal_energy_v4_web.pdf

Krewitt, W., Nienhaus, K., Klessmann, C., Capone, C., Stricker, E., Graus, W., et al.. (December 2019). Role and potential of renewable energy and energy efficiency for global energy supply. Germany.

Lehmann, M,. Karimpour, F., Goudey, C. A., Jacobson, P. T., & Alam M. R.. (July 2017). Ocean wave energy in the United States: current status and future perspectives. *Retrieved from ScienceDirect. Renewable and Sustainable Energy Reviews.*

Li, Y. & Yu, H. (May 2012). A synthesis of Numerical Methods for Modeling Wave Energy Converter–Point Absorbers. *National Renewable Energy Laboratory (NREL).*

Malça, C. M. S. P., Beirão, P J. B. F. N. & Felismina, R. P. (September 2014). Influence of material selection on the structural behavior of a wave energy converter. *AIMS Energy*

Malça, C. M. S. P., Beirão, P J. B. F. N. & Felismina, R. P. (November 2014). Finite Element Analysis of a Spherical Buoy for a Point Absorber Wave Energy Converter. *Renewable Energies Offshore.*

McCormick M E. (1981). Ocean Wave Energy Conversion. *New York: Wiley.*

McNamee, D.A., Legros, A.G., Krewski, D.R. et al. (2009). A literature review: the cardiovascular effects of exposure to extremely low frequency electromagnetic fields.

Mei, C. C. (June 1976). Power Extraction from Water Waves. *Journal of Ship Research, vol. 20.*

Mekhiche, M. (2016). PB500, 500 KW Utility-Scale PowerBuoy Project. *Ocean Power Technologies (OPT).*

Mørk, G., Barstow, S. Kabuth, A. & Pontes, M. T. (2010). Assessing the Global Wave Energy Potential. *Proceedings of OMAE2010: 29th International Conference on Ocean, Offshore Mechanics and Arctic Engineering: Volume 3; 2010 Jun 6–11, ASME Press, Shanghai, China. New York, pp. 447-454*

Muetze, A. Vining, J.G. (October 2006). Ocean Wave Energy Conversion – A Survey. *IEEE Industry Applications Conference Forty-First IAS Annual Meeting*.

Northwest Energy Innovations (2015). Azura Wave. *Retrieved from https://azurawave.com/northwest-energy-innovations-launches-wave-energy-device-in-hawaii/*

Ochi, M. K. & Tsai, C. (2008). Prediction for Occurrence of Breaking Waves in Deep Water. *Journal of Physical Oceanography*.

Ocean Power Technologies (OPT). (2009). Making Waves in Power. *Annual Report for the Year Ended April 30, 2019.*

Owusu, P. A. & Sarkodie, S. A. (April 2016). A review of renewable energy sources, sustainability issues and climate change mitigation.

Penalba, M. & Ringwood, J. V. (2016). A Review of Wave-to-Wire Models for Wave Energy Converters. *Centre for Ocean Energy Research, Maynooth University, Maynooth, Ireland.*

Pelc, R., & Fujita, R. (November 2002). Renewable energy from the ocean. *Marine Policy, Volume 2, Issue 6.*

Polinder, H. & Scuotto, M. (2005). Wave Energy Converters and Their Impact on Power Systems. *2005 International Conference on Future Power Systems*

Reid, J. (1991). The Sideband Instability and the Onset of Wave Breaking. *Breaking Waves: IUTAM Symposium, Sydney, Australia.*

Rusu, E. (June 2014). Evaluation of the Wave Energy Conversion Efficiency in Various Coastal Environments. *Retrieved from http://www.sciforum.net/conference/ece-1/paper/2342*.

Rusu, E. & Onea, F. (2018). A review of the technologies for wave energy extraction, *Clean Energy*, *Volume 2, Issue 1, June 2018, Pages 10–19.*

Rusu, L. & Onea, F. (2017). The performance of some state-of-the-art wave energy converters in locations with the worldwide highest wave power. *Volume 75, pages 1348-1362.*

Sims, R. et al. (2007). Energy Supply. *Climate change 2007: mitigation of climate change, Cambridge University Press, New York, pp. 251-322*

The Queen's University of Belfast. (November 1998). Islay LIMPET Wave Power Plant.

Thomson, C. R., Chick, J. P. & Harrison G. P. (July 1028). An LCA of the Pelamis Wave Energy Converter.

Thomas, J.P. (May 2012). Wave Power: Theory Behind Ocean Waves. *AZO CLEANTECH*.

Thomas, J. T., Barve, K.H., Dwarakish G.S, & Ranganath, L.R. (2015). Review on Assessment of Wave Energy Potential. *National Conference on Futuristic Technology in Civil Engineering for Sustainable Development*

Toledo, E., Ramalho, T. C., & Magriotis, Z. M. (2008). Influence of magnetic field on physical–chemical properties of the liquid water: Insights from experimental and theoretical models.

Torre-Enciso, Y., Ortubia, I., Lopez de Aguileta, L. I., & Marques, J. (January 2009). Mutriku Wave Power Plant: From the Thinking out to the Reality. *Retrieved from* *https://tethys.pnnl.gov/sites/default/files/publications/Torre-Enciso_et_al_2009.pdf*

Toffoli, A. & Bitner-Gregersen, E. M. (2017). Types of Ocean Surface Waves, Wave Classification.

Uihlein, A. & Magagna, D. (2016). Wave and tidal current energy – A review of the current state of research beyond technology.

U.S. Energy Information Administration. (October 2019). Wave Power. *Adapted from National Energy Education Development Project (NEED).*

US Department of Commerce, National Oceanic and Atmospheric Administration, National Weather Service, & National Data Buoy Center. (1996, November 8). National Data Buoy Center. Retrieved from https://www.ndbc.noaa.gov/

U.S Department of Energy. (2019). Powering the Blue Economy: Exploring Opportunities for Marine Renewable Energy in Maritime Markets. *Office of Energy Efficiency & Renewable Energy. Appendices.*

Wave Dragon. (March 2016). Wave Dragon Pre-Commercial Demonstration Project. *Retrieved from https://tethys.pnnl.gov/annex-iv-sites/wave-dragon-pre-commercial-demonstration-project*

Wang, Y., Wei, H. & Li, Z. (March 2018). Effect of magnetic field on the physical properties of water. Volume 8, pages 262-267.

Wang, Y., Zhang, B., Gong, Z. et al. (2013). The effect of a static magnetic field on the hydrogen bonding in water using frictional experiments.

World Health Organization (WHO). (August 2016). Electromagnetic fields and public health. *Retrieved from https://www.who.int/peh-emf/publications/facts/fs299/en/*

World Nuclear Association. (2019). Economics of Nuclear Power.

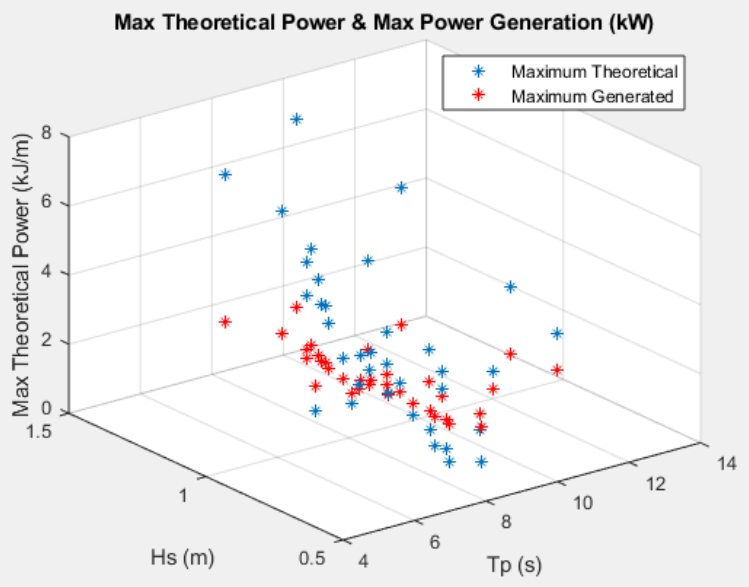
Max Theoretical Power & Max Power Generation (kW)
Maximum Theoretical
Maximum Generated
Max Theoretical Power (kJ/m)
0
2
4
6
8
Hs (m)
1.5
1
0.5
Tp (s)
4
6
8
10
12
14